Materials & Design 266 (2026) 116163

Contents lists available at ScienceDirect

Materials & Design

journal homepage: www.elsevier.com/locate/matdes

# Atomic-scale study of $Cu_3Sn$ and $Cu_6Sn_5$ intermetallic layers growth after soldering

Farzad Khodabakhshi [a,b,c,*], Irina Wodak [a], Shabnam Taheriniya [b], Andriy Yakymovych [a], Michael K. Eusterholz [d,e], Gerhard Wilde [b], Golta Khatibi [a]

[a] Institute of Chemical Technologies and Analytics, Vienna University of Technology, Getreidemarkt 9/164, A-1060 Vienna, Austria
[b] Institute of Materials Physics, University of Münster, Münster 48149, Germany
[c] School of Metallurgy and Materials Engineering, College of Engineering, University of Tehran, P.O. Box: 11155-4563, Tehran, Iran
[d] Institute of Applied Materials (IAM-WK), Karlsruhe Institute of Technology, Hermann-von-Helmholtz-Platz 1, 76344 Eggenstein-Leopoldshafen, Germany
[e] Karlsruhe Nano Micro Facility (KNMFi), Karlsruhe Institute of Technology, Hermann-von-Helmholtz-Platz 1, 76344 Eggenstein-Leopoldshafen, Germany

ARTICLE INFO

*Keywords:*
$Cu_3Sn/Cu_6Sn_5$
Soldering
Thermal aging
Atomistic structure
Nanoscale mechanisms

ABSTRACT

Advanced microscopy and elemental analysis techniques were employed to investigate the atomic-scale characteristics of intermetallic compound (IMC) layers of $Cu_3Sn$ and $Cu_6Sn_5$, which commonly form on copper-based surfaces during reflow soldering with lead-free Sn-based alloys in electronic packaging applications. The study also focused on the influence of iron nanoparticles—introduced via the soldering flux and localized at the interface during solidification—on the growth and coarsening behavior of these IMCs during both reflow and aging processes. High-resolution analyses, comprising atom probe tomography (APT) and scanning transmission electron microscopy (STEM), were used to characterize nanoscale precipitates at interfaces between $Cu_3Sn$ and $Cu_6Sn_5$, as well as between $Cu_6Sn_5$ and the solder joint. These analyses aimed to elucidate the mechanisms by which iron nanoparticles suppress IMC growth during thermal processing. In addition, nanobeam diffraction mapping (NBDM) was used to quantify nanoscale strain distributions at intermetallic interfaces resulting from solid-state phase transformations during soldering. In the thin, fine-grained $Cu_3Sn$ layer, the dominant suppression mechanism was identified as nanoscale segregation of elemental iron. Conversely, in the thicker, coarse-grained $Cu_6Sn_5$ layer, multiple mechanisms were observed. These included solid-solutioning of iron within the complex $Cu_6Sn_5$ crystal structure and *in-situ* reactions with tin, leading to nanoscale $FeSn_2$ precipitates both within the $Cu_6Sn_5$ layer and extending into the solder matrix. Together, these mechanisms contribute to inhibiting IMC growth during soldering and subsequent thermal aging.

## 1. Introduction

The quality of solder joints of lead-free tin-based on copper-based components and their corresponding functionality is strongly reliant on the creation of intermetallics at the joint interface [1,2]. In such systems involving copper as substrate and solder alloys of Sn-based, two distinct intermetallic compound (IMC) layers formation—primarily $Cu_3Sn$ and $Cu_6Sn_5$—is commonly observed and well-documented [3,4]. Thermodynamically, $Cu_3Sn$ is the almost stabilized phase; however, $Cu_6Sn_5$ forms and grows more rapidly due to its favorable kinetics [5]. This kinetic–thermodynamic interplay typically results in a two-layer IMC structure at the solder joint interface [6,7].

Upon post-soldering annealing at elevated temperatures and extended holding times, this $Cu_3Sn/Cu_6Sn_5$ bilayer structure gradually evolves toward a single-phase $Cu_3Sn$ layer, driven by thermodynamic stability [7,8]. The initial chemical and metallurgical bonds across the substrate/solder alloy interface can be established by exhibiting a vital contribution of these IMC layers [9]. Nevertheless, the excessive growth of either layer upon reflow soldering or subsequent thermal modifications can be detrimental to joint reliability. Owing to their inherent brittleness, these IMCs can serve as preferential pathways for crack propagation, leading to premature mechanical failure [10]. Therefore, controlling the formation and growth of $Cu_3Sn$ and $Cu_6Sn_5$—specifically, their thickness ratio, interfacial morphology, and coarsening behavior during aging—is critical for predicting and enhancing the mechanical performance of solder joints [11,12]. An optimal soldering

* Corresponding author..
*E-mail addresses:* farzad.khodabakhshi@tuwien.ac.at, khodabak@uni-muenster.de, fkhodabakhshi@ut.ac.ir (F. Khodabakhshi).

https://doi.org/10.1016/j.matdes.2026.116163
Received 21 August 2025; Received in revised form 30 April 2026; Accepted 2 May 2026
Available online 3 May 2026

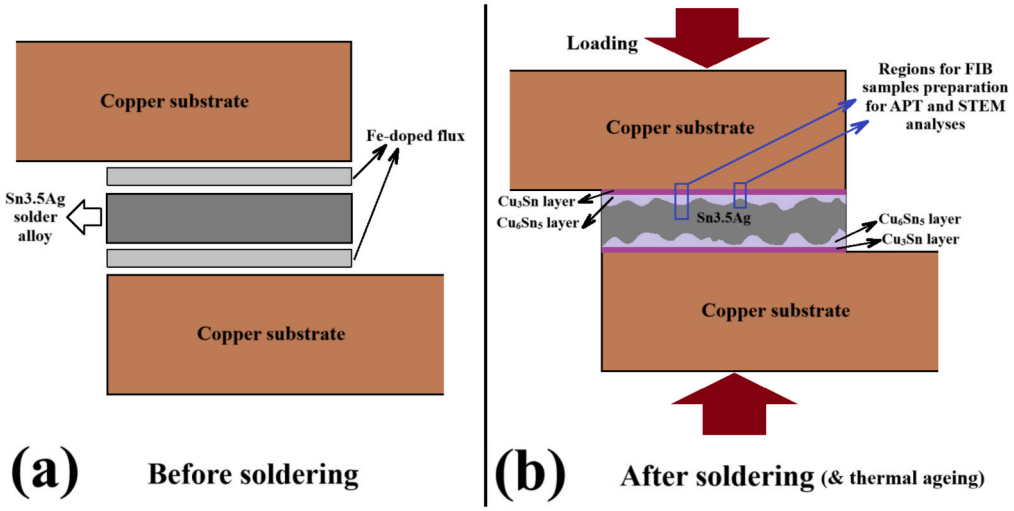


**Fig. 1.** Schematic diagrams illustrate (a) the reflow soldering process using Fe-doped fluxes across both interfaces, and (b) mechanisms for intermetallic layers formation after completion of reflow soldering, solidification, and consequently thermal aging of soldered joints, addressing appropriate regions to extract FIB lamellas from the interface for advanced microscopies.

condition aims to promote beneficial intermetallic bonding while minimizing layer thickness and suppressing coarsening kinetics, thereby improving long-term joint reliability.

The incorporation of secondary phase agents—such as metallic or ceramic nanoparticles—into solder alloys to form solder nanocomposites has emerged as a promising strategy to reinforce the solder matrix, enhance creep resistance, and improve the reliability of microelectronic devices. Moreover, these nanoparticles can directly contribute to the solder joint interface by suppressing the growth kinetics of the intermetallic compound (IMC) layer during reflow solidification [11,13,14]. In the field of lead-free nanocomposite soldering, extensive studies have been conducted, primarily on tin-based systems, using various ceramic reinforcements. These include ceramic oxides [15–19], nitrides [20–22], carbides [23–26], carbon-based nanostructures [27–30], and even metallic nanoparticles [31] such as iron [32,33], cobalt [34], and nickel [35,36]. Over the past three decades, various studies have examined the mechanical reliability of these nanocomposite solder joints, correlating performance with microstructural evolution for microelectronic applications [37,38].

Although varying trends have been reported depending on the type of reinforcing nanoparticle, many microstructural characterizations suggest limited effectiveness of these inclusions at the solder joint interface. This has been primarily attributed to the bubbling phenomenon upon the reflow solidification step, which disrupts the distribution and interaction of the nanoparticles at the critical interface [39–41].

As an alternative approach, nanoparticles can be introduced via the flux material rather than directly into the solder alloy. This method—commonly referred to as doped flux—has recently gained considerable attention in hybrid nanocomposite soldering research [31,42,43]. In this technique, reactive metallic nanoparticles are dispersed in the flux and applied directly at the solder joint interface prior to reflow. Doped fluxes have shown promising results in suppressing IMC growth during reactive soldering processes involving tin-based solders and copper substrates, when implemented with nanoparticles such as Fe [44], Cu [45–47], Co [48–51], Zn [52], or Ni [48,50,53–55].

Because these metallic nanoparticles are precisely positioned at the solder/substrate interface via the flux medium, they can interact more effectively with the forming $Cu_3Sn$ and $Cu_6Sn_5$ intermetallic phases during reflow, thereby influencing their nucleation and growth in a beneficial manner [31,43,56].

The underlying atomistic-scale mechanisms remain insufficiently understood. Despite extensive research on various solder systems, focusing on the hybrid solder joints resulting in microstructures and mechanical reliability [57,58]. The performance of these joints is largely governed by the structure, morphology, and thickness of the intermetallic layers formed across the copper substrate/solder alloy interface [59–61]. However, the fundamental processes controlling their evolution remain poorly understood.

Thermodynamics-based phase-field modeling of solder solidification has been employed to simulate the $Cu_3Sn$ and $Cu_6Sn_5$ phases nucleation and growth, revealing that coarsening behavior for these intermetallics is strongly influenced by solute element drag and trapping along the advancing solid–liquid interface during reflow [62–65]. These solute concentration gradients, established at the boundary across the molten solder and the growing IMC layer, play a critical role in determining the rate and morphology of phase formation [66–68].

In addition to solute transport effects, solid-state phase transformations within the intermetallic matrix—and the potential formation of new *in situ* phases—also significantly impact the growth dynamics and thickening behavior of $Cu_3Sn$ and $Cu_6Sn_5$ [69,70]. These mechanisms are essential for understanding and ultimately controlling the microstructural evolution of solder joints for electronic packaging applications [71].

Building on the above discussions, the principal focus of the current research is to address a key knowledge gap in metal soldering: the nanoscale mechanisms governing the formation and growth of intermetallic phases $Cu_3Sn$ and $Cu_6Sn_5$ at solder joint interfaces with copper substrates. To explore this, reactive hybrid solder joints were fabricated using a doped flux approach. Lead-free Sn-3.5Ag solder was applied between copper substrates arranged in a sandwich configuration [72], with iron nanoparticles introduced into the flux matrix to act as reactive secondary-phase agents at the interface. Sn-3.5Ag is a very popular lead-free solder alloy with widespread applications for joining copper-based connections in the microelectronic industry, which was the main reason the current research focused on modifying this solder alloy by applying Fe-doped flux at the copper substrate interface. The primary reason for selecting Fe-nanoparticles was their reactivity, which facilitated the progression of *in situ* liquid-phase/solid-state chemical reactions, leading to the formation of nanometric secondary-phase precipitates/particles. The high fraction of these new nanophases, formed *in situ*, is expected to significantly benefit the suppression of $Cu_3Sn$ and $Cu_6Sn_5$ intermetallic layer formation and growth during soldering and subsequent thermal aging.

Following optimized reflow soldering cycles and atmosphere-controlled solidification, the joints underwent a standard thermal aging treatment to stabilize their microstructure. The final, reflowed,

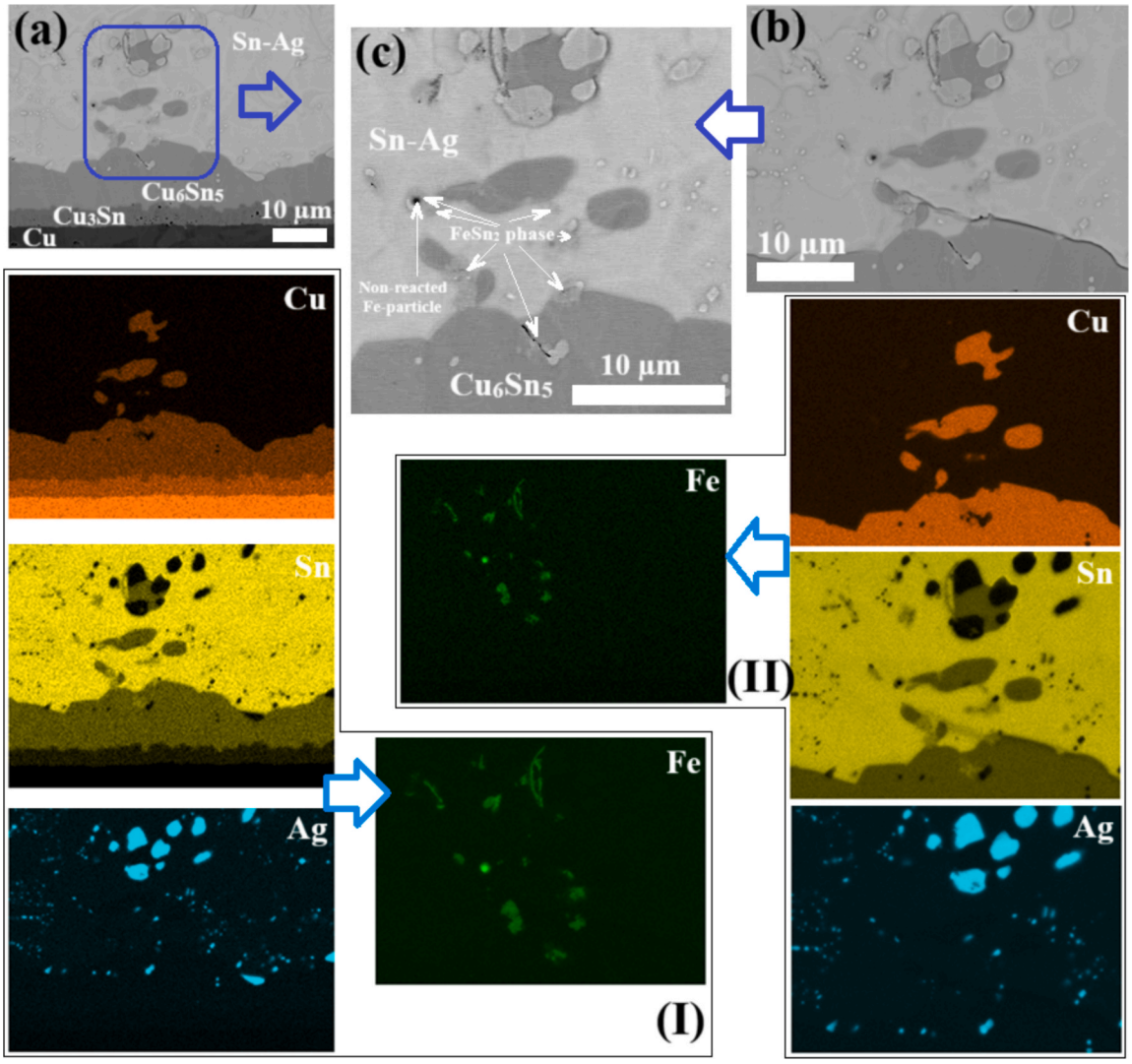


**Fig. 2.** Different views (low- (left) and high-magnification (right)) of the solder joint interface reinforced with 2 wt% Fe nanoparticles, showing the formation of $Cu_3Sn/Cu_6Sn_5$ intermetallic phases, by FE-SEM backscattered electron imaging and EDS elemental mapping analysis. (a) Backscattered image from the overall cross-section of the solder joint, including Cu-substrate, $Cu_3Sn$, and $Cu_6Sn_5$ IMC layers, and the solder alloy, alongside the corresponding EDS elemental map of (I). (b, c) Z-contrast phase structural FE-SEM images at two different magnifications from the interface of $Cu_6Sn_5$ IMC layer with the solder alloy matrix, combined with the corresponding EDS analysis map of (II).

and aged hybrid nanocomposite joints were then subjected to advanced microscopy techniques to investigate the atomic-scale mechanisms underlying the nucleation and growth kinetics of the intermetallic layers that generate the $Cu_3Sn$ and $Cu_6Sn_5$ phases.

Microstructural features, including segregation and alloying behavior of Fe nanoparticles and their clustering within and around the IMC layers, have been characterized using field-emission scanning electron microscopy (FE-SEM) with energy-dispersive X-ray spectroscopy (EDS) and electron channeling contrast imaging (ECCI) for grain/phase analysis. Targeted regions at the $Cu_3Sn/Cu_6Sn_5$ interfaces—adjacent to both copper substrate and solder alloy—were extracted using focused ion beam (FIB) milling in high-resolution analysis.

Scanning/transmission electron microscopy (S/TEM) and atom probe tomography (APT) are advanced techniques for examining atomic-scale structure, intermetallic layers, elemental composition, and surrounding interaction zones. In addition, nano-beam diffraction mapping (NBDM) within STEM was used to measure localized nanoscale strain distributions across the IMC layers, their grain boundaries, and embedded nanoprecipitates.

The thicknesses of these $Cu_3Sn$ and $Cu_6Sn_5$ IMC layers and the corresponding activation energies were measured and discussed in the previous work [72], revealing a higher activation energy required for their growth and coarsening due to the incorporation of these iron nanoparticles. The focus of the current study, as emphasized in the topic, is on the atomic-scale study of intermetallic layers and their interactions with iron nanoparticles, using advanced analytical techniques, including STEM/HR-TEM and APT. Based on the results from these advanced characterization methods, the study provides a detailed discussion of the atomic-level mechanisms driving the formation and evolution of $Cu_3Sn$ and $Cu_6Sn_5$, as well as their nanoscale interactions with alloyed Fe nanoparticles.

## 2. Materials and experimental methodologies

### 2.1. Fabrication of nanocomposite solder joint

The hybrid solder joint design investigated in this study involved applying doped flux to both interfaces between the solder and the copper substrates before soldering. To prepare the doped flux,

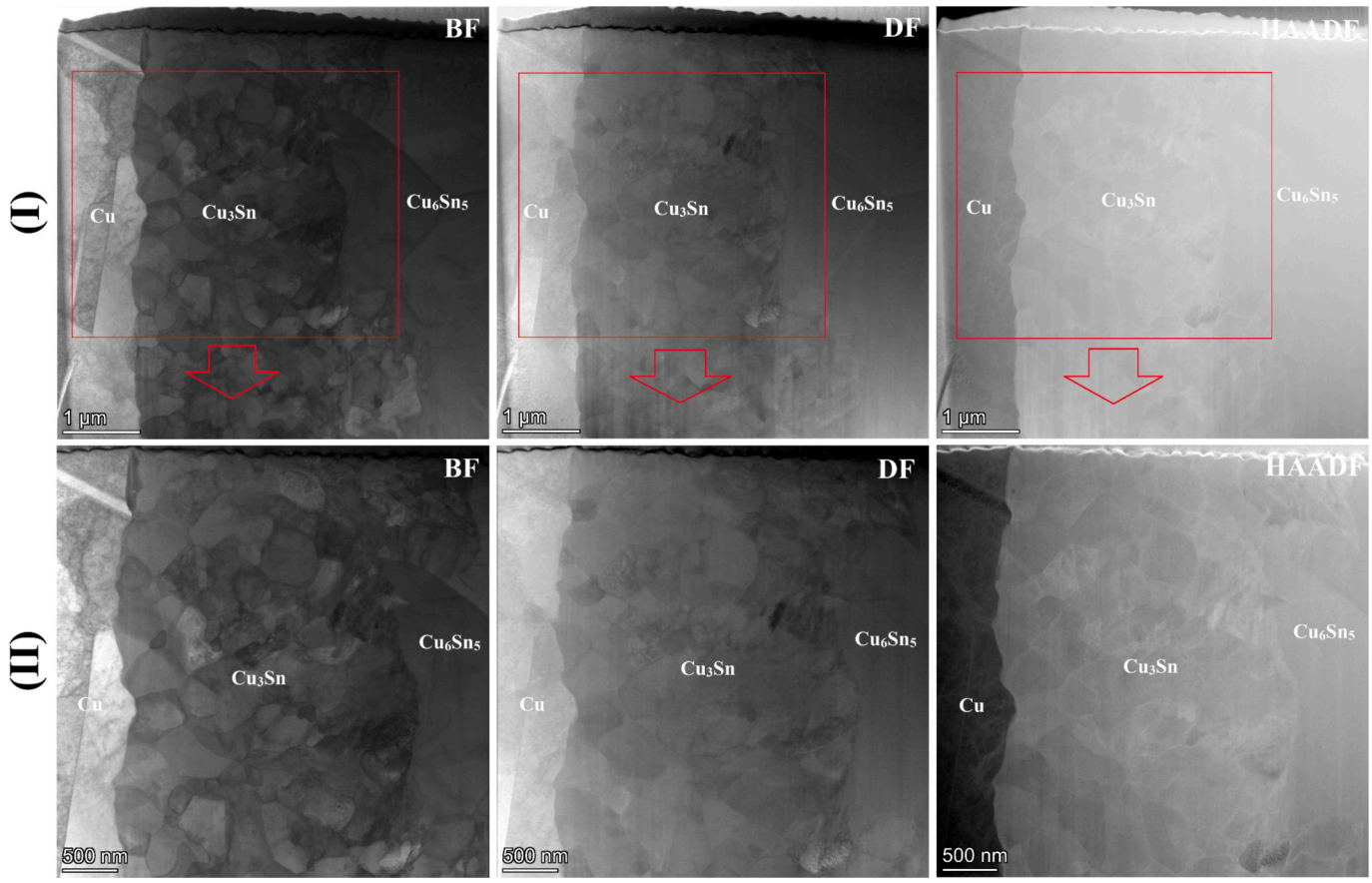


**Fig. 3.** STEM nanostructures under BF, DF, and HAADF contrast imaging modes from the interface region between three different phases of Cu, $Cu_3Sn$, and $Cu_6Sn_5$, at two different magnifications, shown in parts (I) and (II).

approximately 2.0 wt% of high-purity iron nanoparticles (purity > 99.5%, particle size < 50 nm) were uniformly dispersed within a commercial MULTIFIX flux matrix using an attrition milling system. Following oxide removal by mechanical grinding and surface cleaning with ultrasonic treatment in isopropanol/methanol, a doped flux thin layer has been introduced on the cleaned copper substrates. A Sn-3.5 wt % Ag alloy foil, 200 μm in thickness, was used as the solder material. The joint assembly followed a sandwich design, with a ~ 0.2 mm gap maintained between the copper substrates to facilitate reflow soldering. As previously discussed, introducing iron nanoparticles into the solder interfaces via a doped flux, with a defined amount delivered via a syringe, was intended to mitigate the formation and coarsening of intermetallic layers ($Cu_3Sn$ and $Cu_6Sn_5$) during both reflow soldering and subsequent thermal aging.

Based on previous experimental trials [44,72] on the same Sn-3.5Ag solder alloy (lead-free) system incorporating iron nanoparticles, the maximum amount of 2.0 wt% Fe nanoparticles was homogeneously distributed throughout the flux. Above this amount, the mixing and fluxing method applied in this research suggests that the nano-agents may aggregate through the doped flux, potentially reducing their effective contribution across the solder joint interface and suppressing the formation and growth of intermetallic layers. The weight fraction of Fe nanoparticles in the flux matrix was carefully measured by weighing the flux and nanoparticles to high precision. Meanwhile, after applying these Fe-doped fluxes at the solder joint interface with the copper substrate, it is not possible to report the actual content of these nanoparticles at the joint interface, since the nanoparticles and their decomposition products generated by the fluxing procedure would be confined to the interface. This matter can significantly affect the growth and thickness of $Cu_3Sn$ and $Cu_6Sn_5$ intermetallics.

After assembling the joint with an approximate area of ~ 12 $mm^2$ and securing it with solder foil and doped flux under light compressive pressure (<100 N) in a precision alignment die, the configuration was placed in an atmosphere-controlled furnace with real-time temperature monitoring. A preheating stage at 160°C for 300 s was used to activate the flux and ensure good interfacial contact. This was followed by a reflow stage at 270°C, maintained for up to 300 s, to complete the solder melting and solidification. After cooling to room temperature, the joint was thermally aged at 180°C for up to 480 h to simulate long-term service conditions and promote stabilization of the intermetallic phase. The applied temperatures and times used in this research for reflow soldering, as well as for thermal aging afterward, were selected based on optimizations from previous research [44,63]. In this context, the optimized soldering temperature and time were minimized for copper substrates after the soldering process was completed. Regarding the temperature and time range for thermal aging treatment after the soldering process, these are primarily determined by the application field of copper assemblies for electronic connections and the expected heating cycles in the corresponding industrial applications.

Fig. 1 illustrates the schematic diagrams for solder joint assembly (left side, Fig. 1a) and the mechanism of intermetallic layers formation by incorporation of Fe-nanoparticles after reflow soldering and subsequent thermal aging treatment (right side, Fig. 1b). The resulting hybrid solder joints were then subjected to advanced microscopy and nanoscale analysis, forming the core of this research. These investigations aimed to uncover and explain the atomic-scale mechanisms and interactions driving the formation and growth of intermetallics in interfacial layers undergoing the impact of reactive iron nanoparticles.

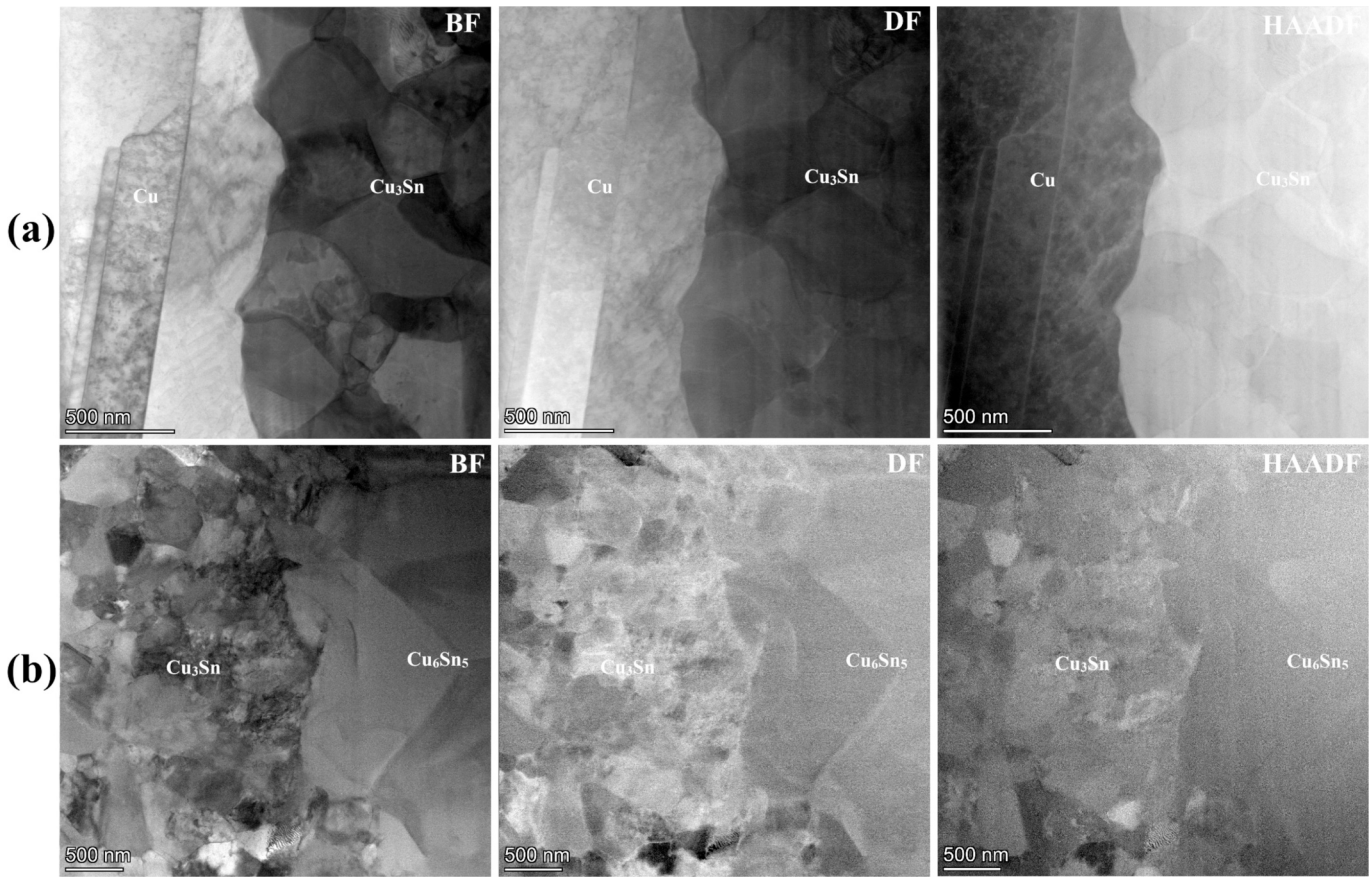


**Fig. 4.** High-magnification BF, DF, and HAADF STEM images illustrating the structure of nano-grains for two interfaces of (a) $Cu/Cu_3Sn$, and (b) $Cu_3Sn/Cu_6Sn_5$.

### *2.2. Advanced electron microscopy characterizations*

Following sectioning of the central region of the soldered joint using a precision micro-cutter, the cross-sectional specimen was cold-mounted in a copper-particle-reinforced epoxy resin to ensure conductivity. Standard metallographic preparation procedures were then carried out, involving sequential grinding and polishing using an automated system to achieve a mirror-like surface finish. To eliminate any mechanically damaged surface layer, final polishing was performed using a vibratory polishing machine with a nanometric colloidal silica suspension ($SiO_2$, ~20 nm particle size) for up to 15 min. This step ensured a high-quality surface suitable for nanoscale characterization.

The formation of intermetallic layers of the $Cu_3Sn$ and $Cu_6Sn_5$ phases at the solder joint interface, along with the micro-scale distribution of iron nanoparticles introduced as alloying agents, was examined using field-emission scanning electron microscopy (FE-SEM). Elemental mapping was performed using energy-dispersive X-ray spectroscopy (EDS) to assess the chemical composition across the joint. These analyses were performed using a JSM-7600F FE-SEM (JEOL), well-appointed with an EDS detector from Oxford Instruments. Backscattered electron imaging mode was employed to highlight electron channeling contrast and reveal detailed microstructural features across different regions of the solder joint.

To achieve higher-resolution characterization and overcome the limitations of the interaction volume inherent in FE-SEM/EDS analysis, the previously prepared and polished specimen was used to prepare a thin lamella via focused ion beam (FIB) milling, followed by scanning transmission electron microscopy (STEM) analysis. In this case, interested regions for FIB lamellas preparation of soldered joints cross-sections with thicker and thinner intermetallic layers are also indicated on the schematic diagram of Fig. 1b. A ZEISS FIB/FE-SEM instrument equipped with a focused gallium ion beam was utilized to prepare lamellae with a thickness below 100 nm, extracted from critical interfacial areas for nanocomposite solder connection—encompassing Cu-based metal, $Cu_3Sn$ and $Cu_6Sn_5$ intermetallics, and Sn-3.5Ag solder alloy.

Due to the considerable thickness of the $Cu_3Sn$ and $Cu_6Sn_5$ layers, a single lamella could not fully capture the interface while maintaining the required nanometric thickness. Therefore, two separate lamellae were prepared: one from the $Cu/Cu_3Sn/Cu_6Sn_5$ interfaces, and the other across the $Cu_6Sn_5$/Sn-3.5Ag solder interaction border.

Subsequent STEM analysis was conducted using a Titan Themis G3 FEI microscope. Imaging was performed at various magnifications using multiple modes—comprising bright-field (BF), dark-field (DF), and high-angle annular dark-field (HAADF)—to examine nanoscale grain structures and phase morphology. STEM/EDS elemental mapping was also performed to assess the chemical distribution of nanoscale features at the interfaces.

To further investigate lattice distortions and local strain fields, nano-beam diffraction mapping (NBDM) was employed on selected interfacial regions. During this analysis, a defined area was scanned at the nano-scale using a focused electron beam, and selected area electron diffraction (SAED) patterns were collected point by point across the scan field. Using a computer-aided algorithm, deviations in the diffraction patterns were analyzed to extract spatially resolved measurements of localized dilation, shear, and rotational strain components. The results were then visualized in both contour maps and directional strain distribution plots to provide a detailed understanding of strain behavior at the nanoscale across the intermetallic interfaces.

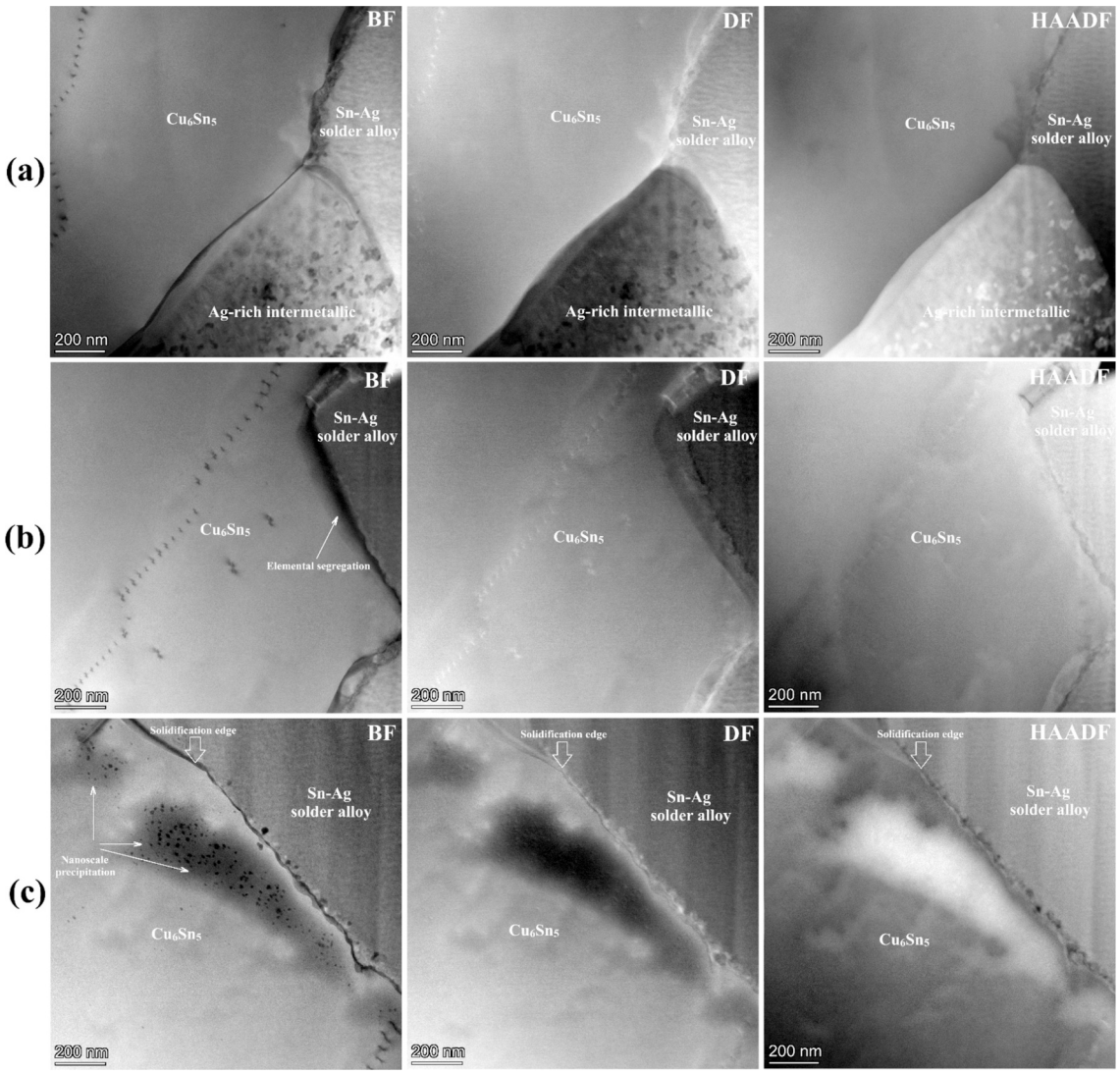


**Fig. 5.** STEM images for three modes of BF, DF, and HAADF from the solidification edge of the intermetallic layer with the solder alloy. (a) A triple-junction between the $Cu_6Sn_5$ layer, Ag-rich intermetallic phase, and solder alloy. (b) The composition gradient interface between the $Cu_6Sn_5$ layer and the Sn-Ag solder alloy. (c) Trapping of secondary phase inclusions inside the $Cu_6Sn_5$ phase and retarding of their formation toward the solder alloy matrix across the solidification phase boundary.

### *2.3. Atom probe tomography (APT) analysis*

As one of the powerful advanced techniques for atomic-scale chemical analysis, APT was employed to investigate the nanoscale structure of the $Cu_3Sn$ and $Cu_6Sn_5$ intermetallic layers and their interactions with the Sn-3.5Ag solder alloy during reflow solidification and succeeding thermal aging. APT tip specimens were prepared via lift-out using the focused ion beam (FIB) system (Zeiss AG, Germany) combined with an Auriga 60 scanning electron microscope (SEM). APT experiments were carried out using a pulsed laser Cameca Instruments LEAP 4000X HR system (WI, USA). For this purpose, a pulse energy of 40 pJ from a 355-nm laser at 100 kHz was used. Upon measurements, the detection limit was controlled at the approximate value of 0.003 ions/pulse, and maintained the sample constant temperature at a value of ~ 50 K. Reconstruction and quantitative assessment of the collected data were accomplished using the AP Suite 6.3.1 software package (Cameca Instruments), allowing for detailed three-dimensional mapping of elemental distributions within the intermetallic phases and at their interfaces.

## 3. Results and discussion

### *3.1. FE-SEM/EDS electron microscopy investigation across the hybrid nanocomposite solder joint*

Fig. 2 presents the backscattered electron (Z-contrast) and electron channeling contrast microstructures captured by FE-SEM, along with the conforming elemental maps by EDS analysis obtained at two different magnifications from the prepared solder joint after long-term aging at 480 h. These results illustrate the formation of $Cu_3Sn$ and $Cu_6Sn_5$ intermetallic compound (IMC) layers across the hybrid solder joint interface following reflow soldering and subsequent thermal aging. The maps also highlight the associated elemental distributions, particularly that of iron nanoparticle clusters originating from the doped flux.

From microstructural observations, the $Cu_3Sn$ layer displays a substantially thinner profile than the $Cu_6Sn_5$ phase. This contrast can be attributed to the relatively faster kinetics of $Cu_6Sn_5$ formation and growth during soldering, despite $Cu_3Sn$ being the thermodynamically more stable phase [7,73]. Additionally, the EDS mapping reveals the formation of Ag-rich intermetallic precipitates dispersed throughout the solder matrix and neighboring the $Cu_6Sn_5$ intermetallic region. These

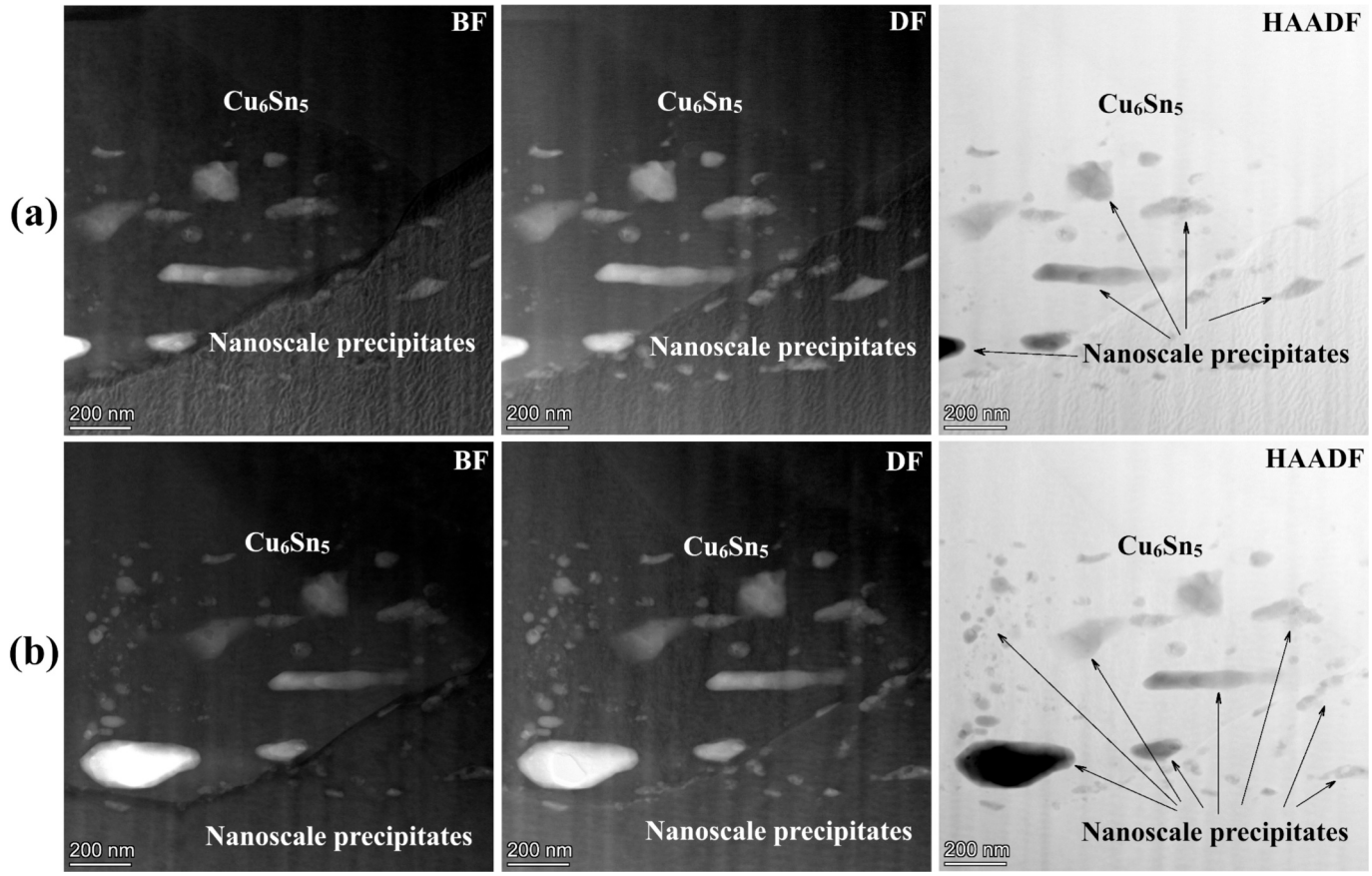


**Fig. 6.** The BF, DF, and HAADF STEM images reveal the distribution of secondary phase nano-scale precipitates within the $Cu_6Sn_5$ intermetallic matrix from two different regions: (a) near the edge of the layer, and (b) behind the layer.

precipitates appear with a variable size distribution and a noticeable volume fraction.

A particularly intriguing observation is the apparent detachment or fragmentation of $Cu_6Sn_5$ particles, likely occurring during IMC formation and coarsening. This phenomenon may be driven by molten solder flow induced by capillary action within the joint clearance, leading to partial displacement of the forming IMC [74,75].

The most notable feature in Fig. 2 is the distribution of iron as revealed by EDS elemental mapping. The iron originates from Fe nanoparticles intentionally incorporated into the flux and applied at the solder–substrate interface prior to reflow soldering. While a minor portion of these nanoparticles appears to remain unreacted, a significant amount either diffuses into the intermetallic layers or reacts to form new phases during soldering and subsequent aging.

The presence of distinct microstructural features and potential new phases within the $Cu_6Sn_5$ intermetallic and in the adjacent solder alloy strongly suggests alloying and *in situ* phase formation involving iron. These preliminary observations point to complex interactions at the nanoscale and highlight the need for advanced microscopy and atomic-level analytical techniques to elucidate further the detailed structural and compositional nature of these transformations. Based on the assessment in Fig. 2, specific agglomeration levels can be identified for iron nanoparticles at the microscale, which will significantly affect their inhibitory effect on the growth kinetics of the $Cu_3Sn$ and $Cu_6Sn_5$ IMC layers. In fact, the uniformity of individual iron nanoparticles' distribution is a crucial factor for their effective interaction with the IMC layers' solidification and subsequent coalescence during thermal aging treatment. As shown in Fig. 2, in the regions where these iron nanoparticles were doped at the interface by applying modified flux, they were clustered as micro-scale features upon soldering reflow solidification; the suppressing contribution seems less significant than in the regions beside, with a nanoscale distribution of iron agents (which is not detectable by FE-SEM/EDS microscopy and analysis due to the interaction volume effect).

### 3.2. *Grain structure of $Cu_3Sn$ and $Cu_6Sn_5$ intermetallics and interfacial bonding by FIB/STEM microscopy*

Fig. 3 illustrates STEM contrast microstructures from three altered contrast modes—BF, DF, and HAADF—focusing on a specific region that includes the interaction zone across $Cu_3Sn$ intermetallic layer/Cu-workpiece, as well as $Cu_6Sn_5$ phase, at two different magnifications. As expected, the $Cu_3Sn$ phase, with an approximate thickness of ~ 2 μm even after annealing and aging treatments, displays an ultra-fine-grained microstructure, with grain sizes ranging from 200 to 500 nm. This thin, nanostructured $Cu_3Sn$ phase, however, is limited in growth due to the concurrent formation of a thicker $Cu_6Sn_5$ layer, which exhibits a coarser-grained microstructure. The STEM images in Fig. 3 clearly show the triple junctions of coarse grains within the $Cu_6Sn_5$ layer, further confirming the coarsening process.

Fig. 4a and 4b show high-magnification BF, DF, and HAADF STEM images of the interfaces between Cu/$Cu_3Sn$ and $Cu_3Sn$/$Cu_6Sn_5$ phases, respectively. In Fig. 4a, the interface between $Cu_3Sn$ and the copper substrate reveals a well-metallurgically bonded region, characterized by a nanometric diffusion layer. Similarly, Fig. 4b, depicting the interface between $Cu_3Sn$ and $Cu_6Sn_5$, shows a distinct transition from nano-crystalline grains on the left to larger micro-sized grains on the right. The interface between these two intermetallic phases also appears well-bonded, with no visible signs of delamination or structural failure.

The subsequent sections will focus on high-resolution structural

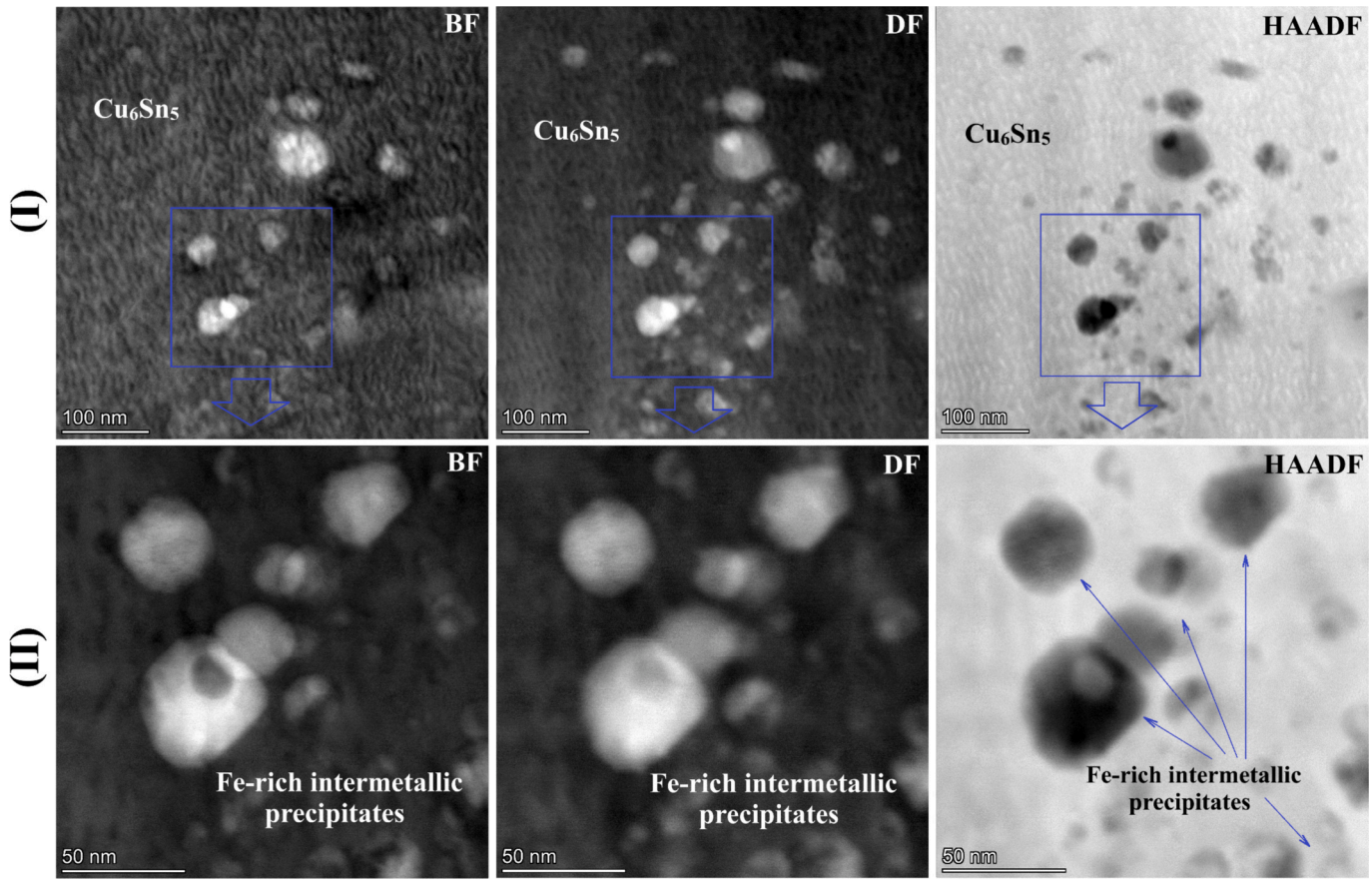


**Fig. 7.** High-resolution BF, DF, and HAADF STEM images of the reacted, roundish nanometric precipitates dispersed throughout the $Cu_6Sn_5$ intermetallic layer at two different magnifications (I) and (II).

characterization of the $Cu_3Sn$ and $Cu_6Sn_5$ intermetallic phases, along with detailed chemical analysis using STEM/EDS elemental mapping to further elucidate their composition and structural evolution.

### 3.3. *Nano-scale aspects through $Cu_3Sn$ and $Cu_6Sn_5$ intermetallic layers*

Fig. 5 presents STEM microscopy images of the growing front of the $Cu_6Sn_5$ IMC phase across the solder alloy matrix interface, along with the silver-rich phase ahead of it, after reflow soldering and thermal aging. The images are shown under three different contrast modes: BF, DF, and HAADF. In Fig. 5a, a triple-junction structure is observed, involving the $Cu_6Sn_5$ intermetallic, Sn-Ag alloy, and Ag-rich phase. Moving to Fig. 5b and 5c, the focus shifts to the interface boundaries across the $Cu_6Sn_5$ intermetallic phase and the solder matrix. These boundaries represent the solidification interface, where a diffuse region with significant elemental segregation is visible, indicating that the incorporated iron nanoparticles hinder the growth of the intermetallic phases. The mechanisms of solute dragging and trapping across the solidification edge are also evident. Fig. 5b highlights the broad range of elemental segregation across this interface, while Fig. 5c reveals the distribution of nanoscale precipitates behind the solidification edge and within the matrix of the $Cu_6Sn_5$ phase. These precipitates, observed in three different contrast modes, exhibit characteristic mass-thickness variations that suggest solid-state interdiffusion of elements and the possible formation of new phases via interfacial chemical reactions, as supported by the solute-trapping theory [36,73].

Further analysis of the nanoscale precipitates formed within the $Cu_6Sn_5$ matrix is presented in Figs. 6 and 7, which show high-magnification BF, DF, and HAADF STEM images of these precipitates from two different locations within the matrix. As seen across all contrast modes, the mass-thickness contrast gradients of these secondary-phase precipitates suggest extensive interdiffusion and the potential *in-situ* formation of new phases via interfacial chemical reactions. Additionally, Fig. 7I and 7II provide high-resolution magnifications of these round precipitates within the $Cu_6Sn_5$ matrix. The observed structural coherence and gradient phase distribution of these nanoscale features indicate that their formation is driven by *in-situ* reactions and atomic-scale diffusion [76,77].

Finally, Fig. 8 presents STEM images of the silver-rich particles at the head of the $Cu_6Sn_5$ intermetallic phase, captured at various locations and magnifications. The images reveal a lamellar or eutectic structure within the Ag-rich phase, likely due to nanoscale elemental segregation. In Fig. 8, region (II) is the top part of the blue box in region (I), and region (III) is the bottom side of that. These observations suggest that further characterization of the newly formed phases and diffusive domains through *in-situ* solid-state chemical reactions will require advanced chemical elemental mapping techniques, such as STEM/EDS and APT, which will be reported in subsequent sections.

### 3.4. *STEM/EDS characterization of nanometric precipitation through the IMC layers*

Fig. 9 presents the HAADF/STEM microstructure of the interface region of the soldered joint, which includes the copper substrate, $Cu_3Sn$, and $Cu_6Sn_5$ intermetallic phases. This is combined with consistent EDS elemental maps showing the spreading of Cu, Sn, Ag, and Fe. By evaluating the STEM/EDS maps of the scanned region, particularly the interaction zone across the $Cu_3Sn$ thin layer/Cu-workpiece and the $Cu_6Sn_5$ phase, valuable insights can be drawn into the interaction of iron nanoparticles with the intermetallic phases during reflow soldering and

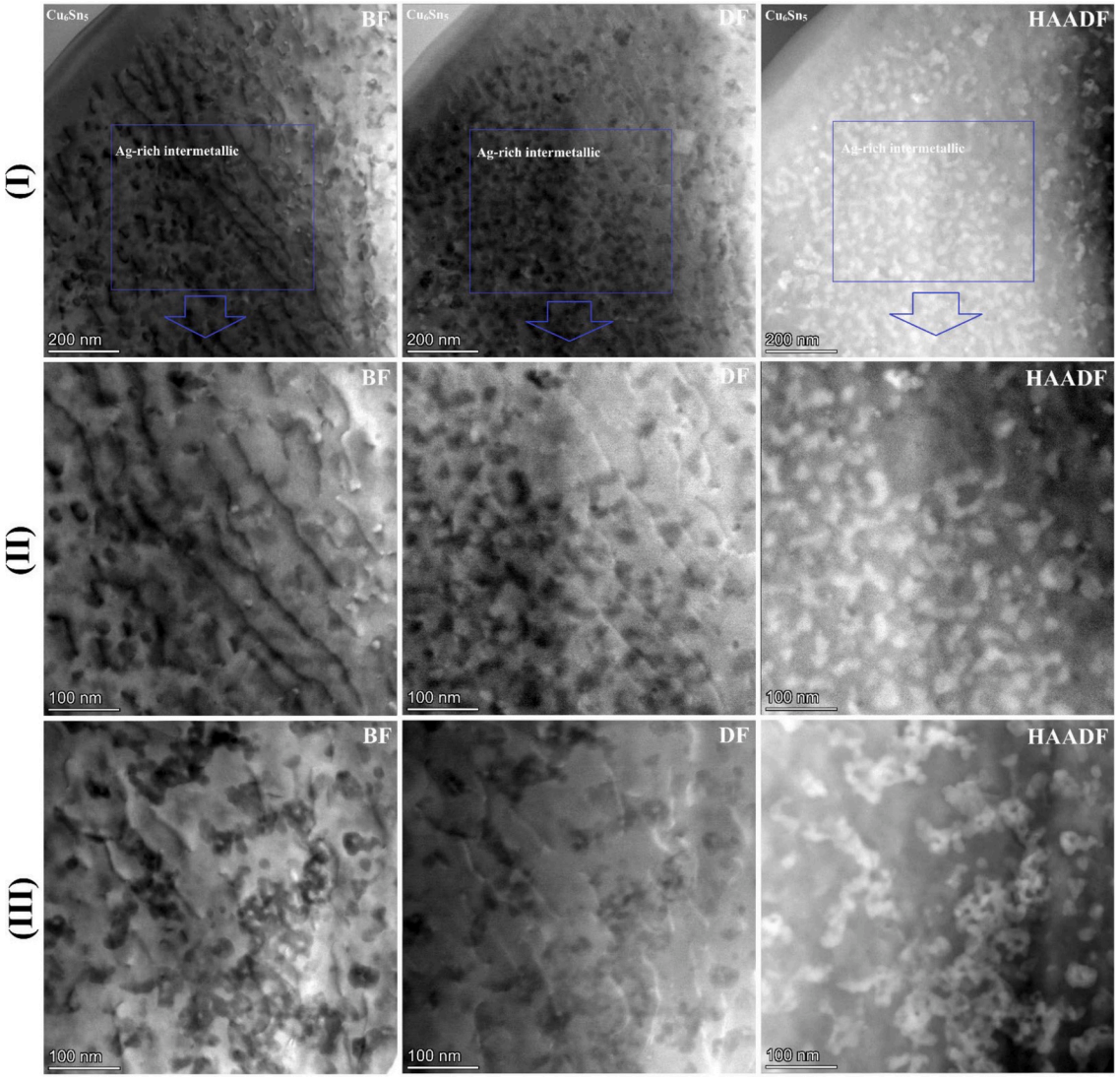


**Fig. 8.** STEM images with BF, DF, and HAADF contrast modes for the nano-scale eutectic/lamellar phase gradients through the structure of an Ag-rich intermetallic particle in front of the $Cu_6Sn_5$ layer at different locations and magnifications, (I), (II), and (III).

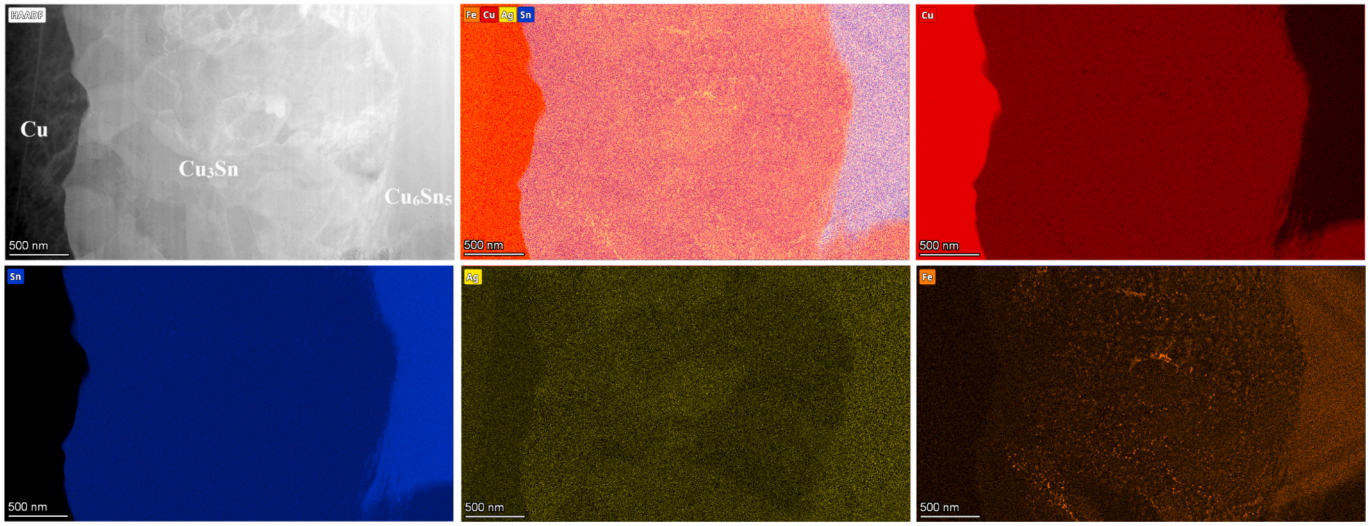


**Fig. 9.** STEM HAADF microstructure combined with the EDS elemental mapping analysis from the interface of $Cu_3Sn$ layer with the copper substrate from the left side and the $Cu_6Sn_5$ intermetallic from the right side, showing the distribution of Cu, Sn, Ag, and Fe elements.

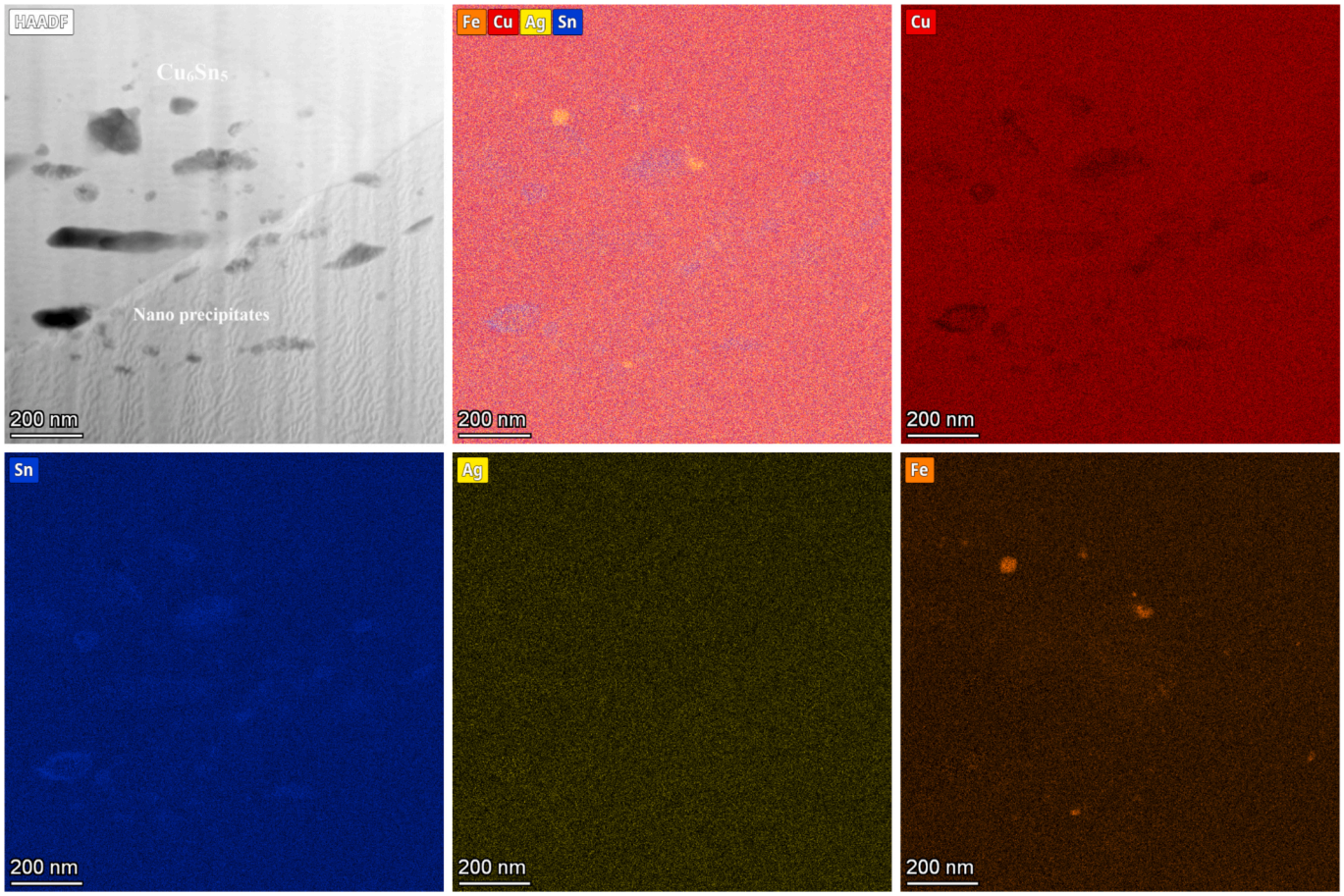


**Fig. 10.** STEM HAADF image and EDS chemical analysis map for the semi-reacted elongated nanoparticles through the matrix of the $Cu_6Sn_5$ intermetallic layer.

subsequent thermal aging.

As shown, the distribution of iron nanoparticles within the $Cu_3Sn$ intermetallic phase primarily manifests as nanoscale segregation, with no significant evidence of iron solid solutioning or alloying within the $Cu_3Sn$ phase. In contrast, a slight incorporation of iron as a solid solution alloying element is observed within the $Cu_6Sn_5$ intermetallic phase, particularly in the thicker region of this layer. This suggests that iron contributes to the phase growth and can form secondary structures in the $Cu_6Sn_5$ matrix.

Figs. 10 and 11 present STEM/EDS elemental maps of the leading edge of the $Cu_6Sn_5$ intermetallic phase, highlighting the distribution of nanoscale precipitates in two regions. In the region closer to the trailing edge of the $Cu_6Sn_5$ phase, near the interface with the $Cu_3Sn$ intermetallic phase (as illustrated in Fig. 9), the iron element shows partial reaction and segregation, forming precipitates within the $Cu_6Sn_5$ phase matrix. This suggests that, in addition to solid solutioning, iron nanoparticles react with other elements during reflow soldering and thermal aging, forming secondary precipitates. Analysis of the STEM/EDS maps for iron and tin reveals that a portion of the primary iron nanoparticles remained non-reacted or only partially reacted, with a diffused gradient. This reaction is likely controlled by diffusion rates, temperature, and processing time [78]. The enrichment of tin around these reacted iron nanoparticles suggests the possible formation of the intermetallic $FeSn_2$, which is the most thermodynamically stable phase in the Cu-Sn-Ag-Fe system [79]. This $FeSn_2$ phase formation and its distribution during reflow soldering and thermal aging could influence the growth and morphology of the $Cu_6Sn_5$ intermetallic layer. The *in-situ* formation of this intermetallic phase around the non-reacted iron particles is demonstrated in the FE-SEM images of Fig. 2, supported by EDS elemental analysis and further details in the previous work [72].

Fig. 12 shows STEM/EDS elemental maps from a silver-rich particle interface with the $Cu_6Sn_5$ intermetallic phase. Since silver has no solubility in the structures of $Cu_3Sn$ and $Cu_6Sn_5$ intermetallics, it will be retarded from the solidification front upon completion of reflow soldering. As shown in FE-SEM images and EDS maps of Fig. 2 and also STEM images of Fig. 5a and Fig. 8(I) to 8(III), alongside the STEM/EDS map of Fig. 12, Ag segregated as the micron- and nano-scale particles within the solder alloy matrix. As previously noted in Fig. 8, the silver-rich phase exhibits a lamellar or eutectic structure, which is further supported by these EDS maps. The structure results from the partial segregation of alloying elements and the diffusion of tin through the silver-rich phase, potentially leading to the formation of $Ag_3Sn$ intermetallic precipitates [80,81]. In the HAADF microstructure of Fig. 12, the white-colored islands represent areas enriched with Ag, while the gray-colored continuous matrix regions indicate the paths of tin diffusion through the silver-rich phase. There are also traces of copper diffusion into the silver-rich phase, but no diffusion of iron is observed within this region.

In this context, as evident and indexed by FE-SEM/EDS results in Fig. 2 and STEM/EDS microscopies in Figs. 5, 8-12, $Ag_3Sn$ precipitation can happen with a high fraction within the matrix of the solder alloy and around the IMC layers' regions, which could affect the growth of these intermetallics. Meanwhile, it is notable that typical $Ag_3Sn$ phase precipitation in the Sn3.5Ag solder alloy system occurs at the micron-scale. This contributes less to the retarding influence on the IMC layers than nanoscale phases, such as Fe nanoparticles, which can form *in situ* new nanometric phases. Also, these $Ag_3Sn$ intermetallic particles are homogeneously distributed throughout the solder alloy matrix across the joint, rather than being particularly concentrated at the interface. However, the contribution of Fe-nanoparticles is primarily at the joint

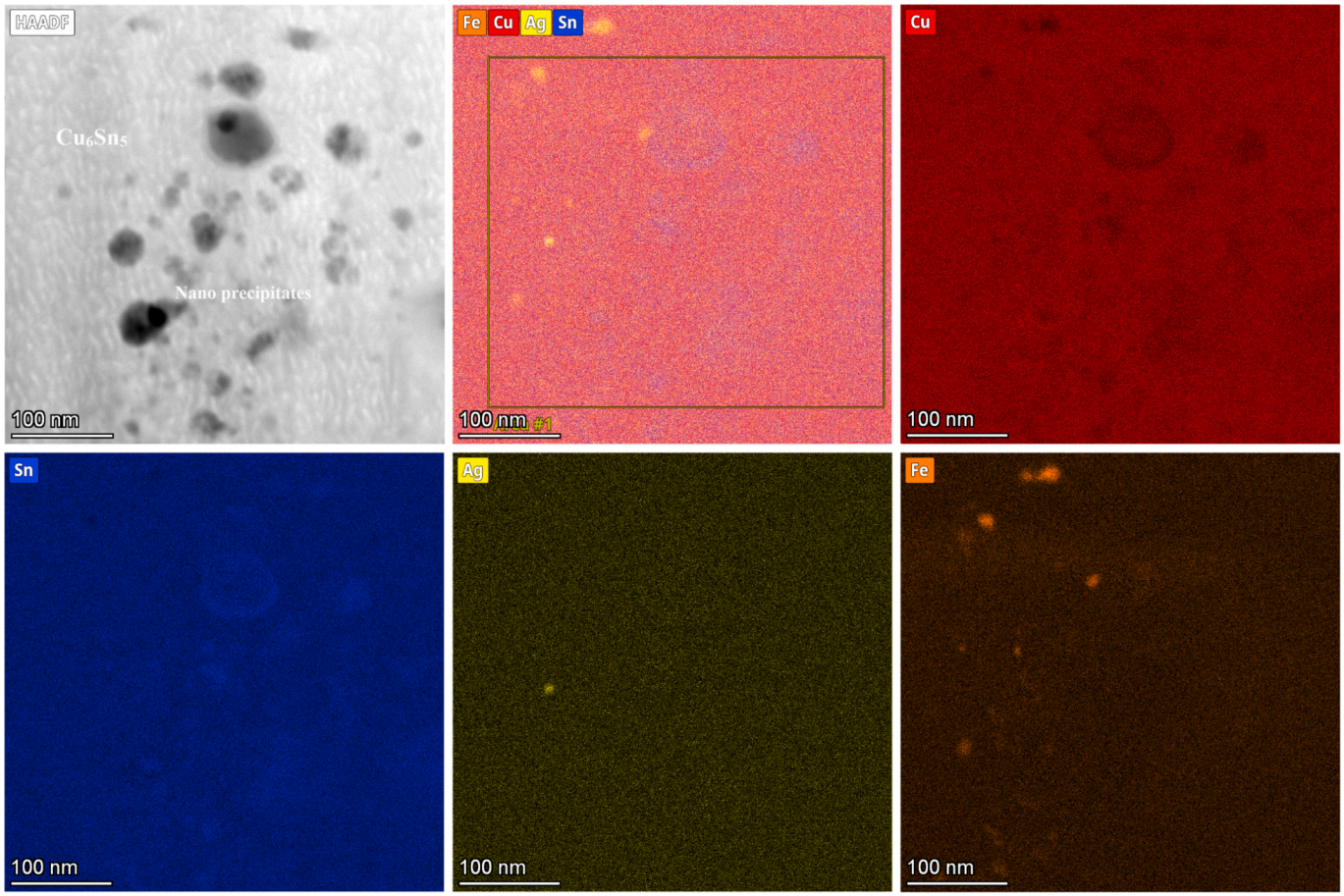


**Fig. 11.** High-magnification STEM image in HAADF mode and the corresponding elemental analysis results by EDS mapping from the reacting roundish nano-scale precipitates within the $Cu_6Sn_5$ matrix.

interface, as it is applied through a doped flux across the solder joint interface.

### 3.5. *Atomic-scale elemental analysis of $Cu_3Sn$ and $Cu_6Sn_5$ intermetallics by atom-probe tomography*

Fig. 13 presents the FE-SEM electron channeling-contrast microstructure of the soldered joint cross-section, illustrating the $Cu_3Sn$ and $Cu_6Sn_5$ intermetallic layers at the Cu-workpiece/solder alloy interface. This figure also highlights regions designated for APT tip sample preparation. As shown in the channeling contrast image in the center of the figure, an initial lamella was prepared from the interaction zone using FIB, incorporating the copper base metal, $Cu_3Sn$, and $Cu_6Sn_5$ intermetallic phases, and the solder alloy. This lamella was then sliced and further thinned using FIB to produce nanometric tips from different phases suitable for APT analysis, as depicted in Fig. 13.

Fig. 14 displays the APT atomic-scale elemental mapping results for the $Cu_3Sn$ intermetallic layer. As expected and consistent with the STEM/EDS elemental maps in Fig. 9, segregation of iron nanoparticles is observed within the $Cu_3Sn$ phase structure following reflow soldering and thermal aging. Figs. 15 and 16 show the APT atomic-scale elemental maps of the thick $Cu_6Sn_5$ intermetallic layer, obtained from the middle and front regions, respectively. These maps, which align well with the previous STEM/EDS results in Figs. 9-11, show that all elements, particularly iron, are distributed homogeneously throughout the $Cu_6Sn_5$ phase. Line-scan analysis reveals that the Cu: Sn atomic ratio fits well with the stoichiometry of the $Cu_6Sn_5$ phase.

Interestingly, the atomic percentage of iron at the front of the $Cu_6Sn_5$ layer (~0.713%) is higher than in the middle region and in the initial portions closer to the Cu3Sn layer (~0.19%), as shown in the APT results of Figs. 15 and 16. This observation aligns with the solidification path model previously described for the reflow soldering process [82,83]. As the $Cu_6Sn_5$ phase grows during reflow solidification, iron nanoparticles are either retarded or trapped at the solidification edge/boundary, where they interact with the tin-based molten solder matrix. Within nucleating regions of the $Cu_6Sn_5$ layer, iron contributes to solid solution formation within the phase structure (see APT elemental distributions in Fig. 15). At the leading edge of this phase, although iron remains in solid solution with a higher atomic fraction, there is a possibility for *in situ* chemical reactions with iron nanoparticles at the edge of the growing $Cu_6Sn_5$ phase. This could lead to the nano-scale precipitation of the $FeSn_2$ intermetallic phase through $Cu_6Sn_5$ structure or across the solder alloy matrix and the $Cu_6Sn_5$ phase interface, as previously characterized in the STEM/EDS maps of Figs. 10-12.

Fig. 17a presents the APT elemental map for the solder alloy at the nanoscale, while Fig. 17b shows the corresponding Sn-Ag phase diagram [84,85]. For Sn-3.5 wt% Ag solder alloy, which has no solubility between Sn and Ag at room temperature, a separated eutectic structure is expected, consisting of two phases, with a much higher fraction of the tin phase than the silver phase. $Ag_3Sn$ intermetallic regions formation across the tin/silver phases interface is also possible, depending on the solid-state kinetics during phase formation [81]. As shown in Fig. 17a, the tip prepared from the Sn-rich phase shows a high tin atomic percentage (>99.94%) and only trace amounts of oxygen. A slight oxygen trapping (less than 0.06 atomic percent) is detected, indicating a concentration gradient due to the reflow soldering process.

The silver phase, previously characterized as micro-sized particles in the FE-SEM/EDS microstructures of Fig. 2 and analyzed in detail in the

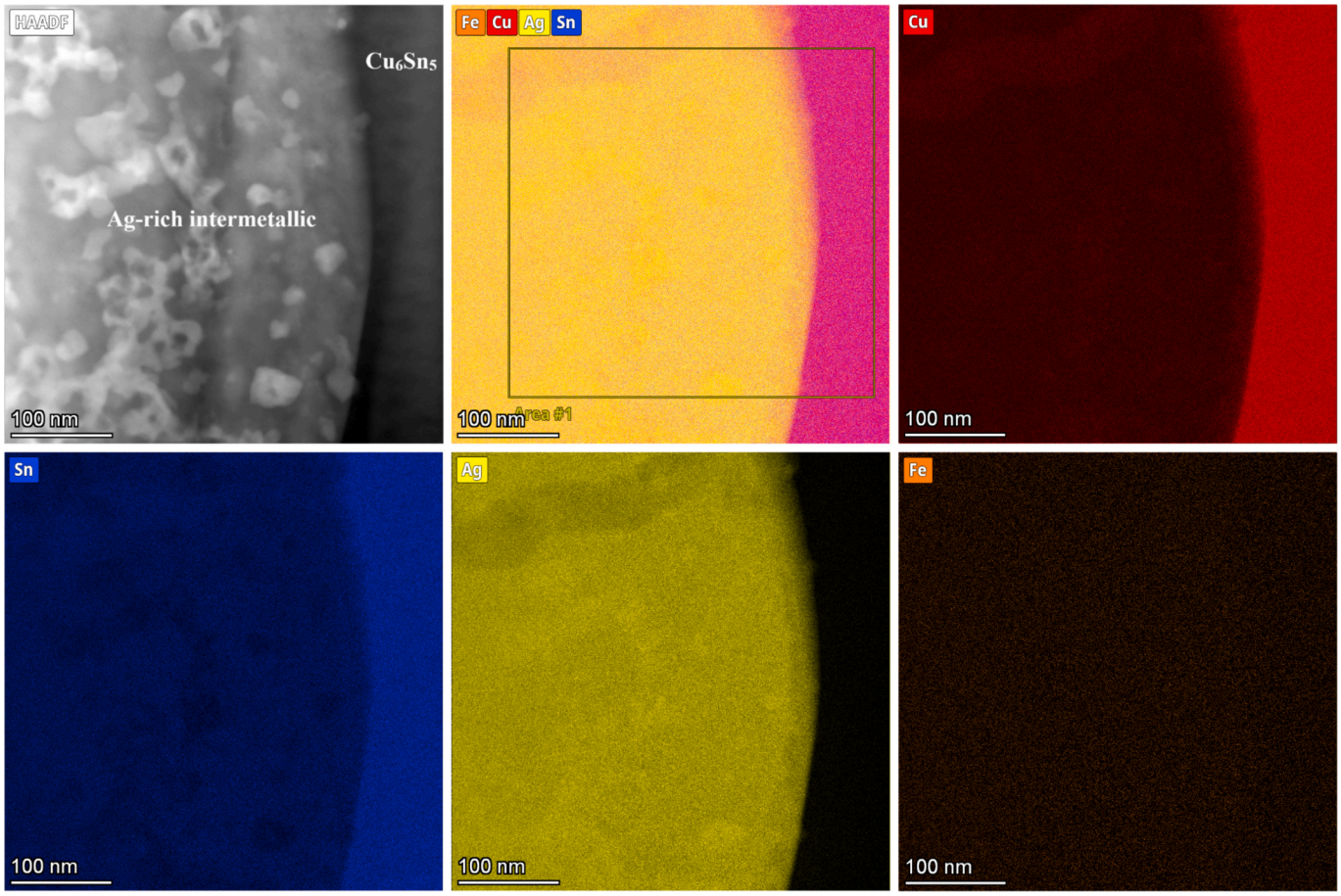


**Fig. 12.** The HAADF STEM/EDS microstructure and map for the phase structure of an Ag-rich intermetallic precipitate and its graded boundary line with the $Cu_6Sn_5$ layer.

high-magnification STEM images of Figs. 5 and 8, is further analyzed in the EDS map of Fig. 12. The silver phase forms secondary precipitates with varying size distributions throughout the solder matrix and partially through the $Cu_6Sn_5$ intermetallic layer.

### *3.6. Strain distributions across the $Cu_3Sn$ and $Cu_6Sn_5$ IMC layers by nano-beam diffraction mapping (NBDM) analysis*

The internal stresses within the intermetallic layers of solder joints are crucial for controlling their brittleness and overall mechanical performance. The primary contribution of internal strain would be to the mechanical durability of soldered joints during cyclic heating and cooling in real-world service for potential microelectronic connection applications. Higher levels of internal strain and steeper gradients across potential interfaces could increase the risk of thermally under-designed fatigue fracture in connections. Therefore, the localized strain distributions of the $Cu_3Sn$ and $Cu_6Sn_5$ phases were analyzed at both interfaces and grain boundaries. As previously mentioned, the results presented in Figs. 18 and 19 represent the first reported application of the nano-beam diffraction method (NBDM) for strain calculation using STEM microscopy for the $Cu_3Sn$ and $Cu_6Sn_5$ intermetallic phases typically formed during soldering. Fig. 18 provides an overview of the key findings for nanoscale localized strain measurements, using NBDM analysis of SAED patterns (demonstrated in Fig. 18a) across the phase boundary between the $Cu_3Sn$ and $Cu_6Sn_5$ intermetallic layers. The strain mapping contours in Fig. 18b-d cover two distinct boundaries within the scanned area.

The first boundary is located between the intermetallic phases of $Cu_3Sn$ and $Cu_6Sn_5$, shown on the left side of the strain contour maps. This boundary displays a sharp transition in localized strain from compressive strain in the $Cu_3Sn$ phase to tensile strain in the $Cu_6Sn_5$ phase. As illustrated, three strain components—dilatation, shear, and rotation—were estimated and mapped based on crystal lattice distortions and deviations in the corresponding SAED patterns.

The second interface is between coarse grains of the $Cu_6Sn_5$ phase, as indicated in the strain contours of Fig. 18b-d. The linear strain distribution profiles for the different components—dilatation, shear, and rotation—across the grain boundary are plotted as a function of position. As expected, strain variations across the two $Cu_6Sn_5$ grains are not significantly different. However, in two small regions adjacent to the grain boundary, notable depletions of the dilatation and shear components from their maximum tensile values, and a shift in the rotation component from its compression value, can be observed. These variations are likely due to structural relaxation near the grain boundary, driven by the high misorientation and irregularity at the boundary.

Fig. 19 shows nanoscale strain mapping of an area containing dispersed iron nanoparticles and newly formed phases within the $Cu_6Sn_5$ intermetallic matrix. The strain distribution reveals significant variations around the secondary phase precipitates, which can be attributed to the degree of incoherence and misfit between these nanometric phases and the $Cu_6Sn_5$ matrix. For larger precipitates, such as the one at the bottom of the selected region, the dilation and shear strain components show negative values relative to the $Cu_6Sn_5$ matrix. In contrast, for smaller, nanoscale precipitates in the region, these strain components shift toward positive values. These broad fluctuations in localized strain around the precipitates, as identified by nanobeam diffraction analysis, are likely linked to the formation of the $FeSn_2$ intermetallic phase and *in-situ* chemical reactions at the interface, which contribute to the crystal lattice mismatch between the gradient-

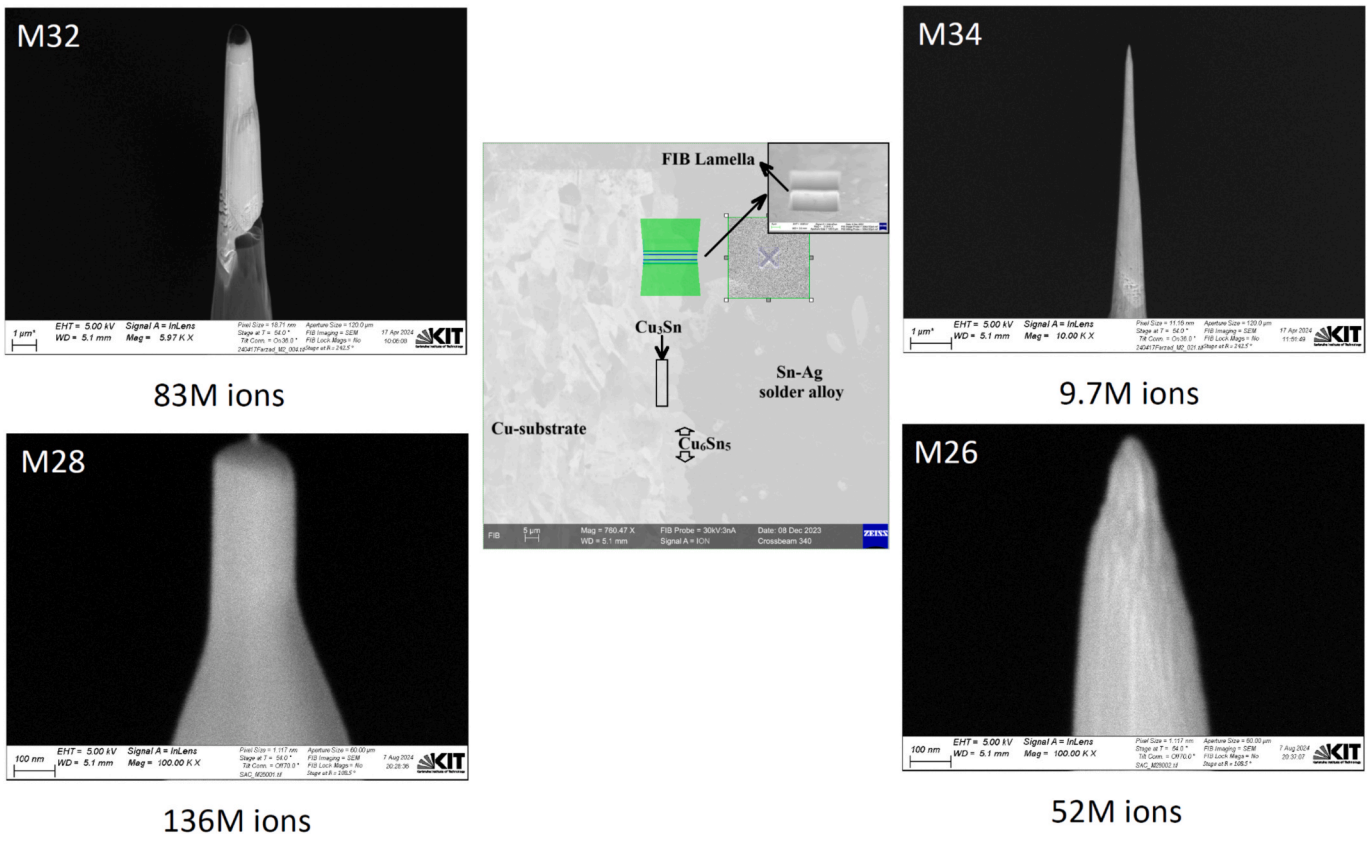


**Fig. 13.** FE-SEM channeling contrast microstructure demonstrating the region of interest selection across the solder joint and FIB preparation of APT tips from different locations concerning the intermetallic layers: $Cu_3Sn$, $Cu_6Sn_5$, and the Sn-Ag solder alloy.

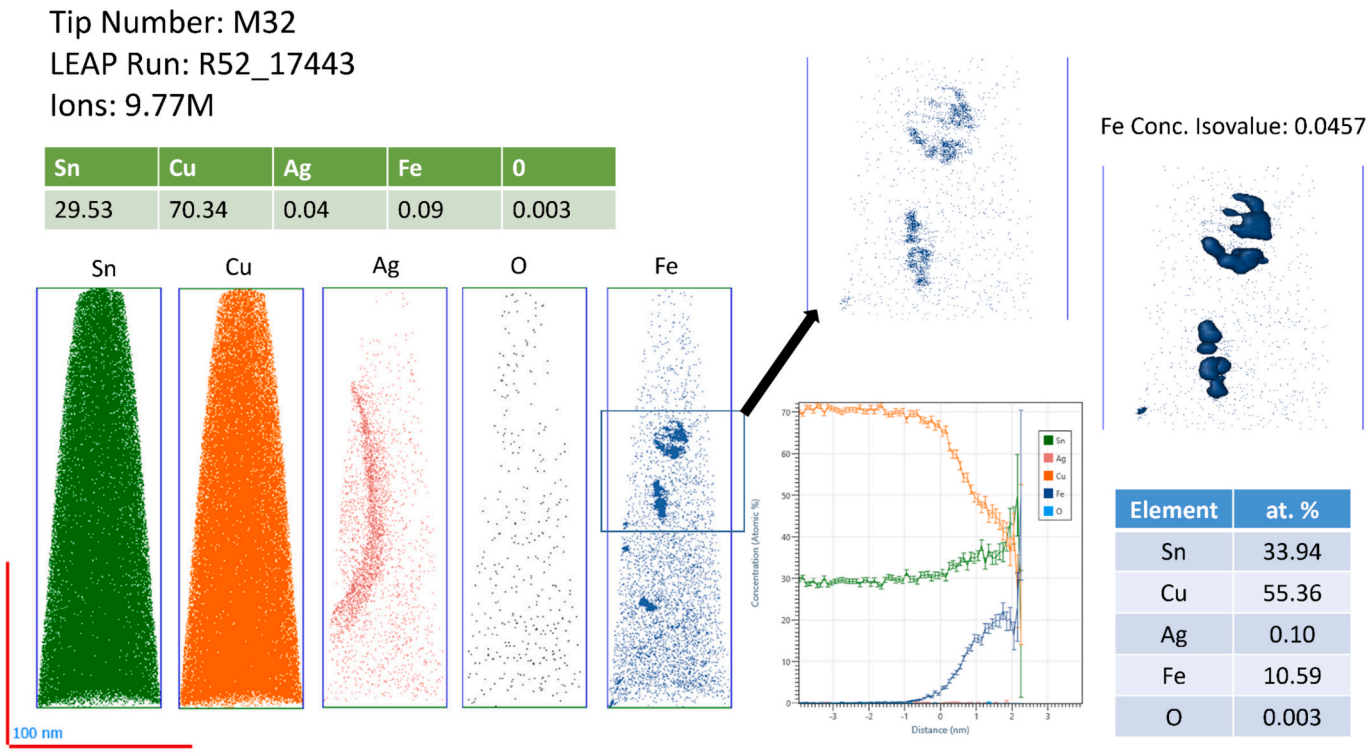


**Fig. 14.** APT elemental analysis results for the tip prepared from the $Cu_3Sn$ intermetallic layer.

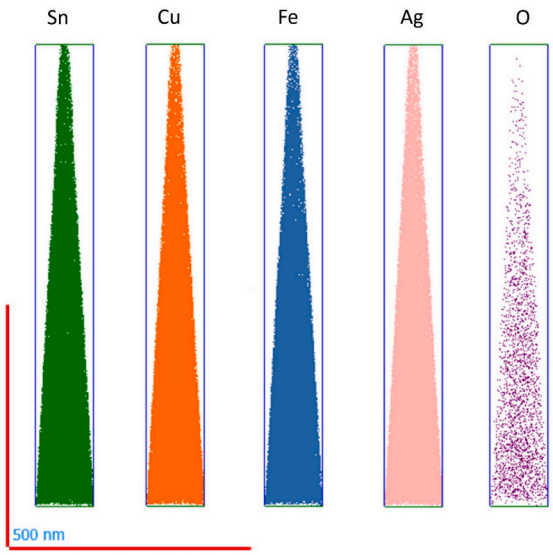


Tip Number: M34
LEAP Run: R52_17447
Ions: 83M

| Element | at. % |
|---|---|
| Sn | 48.78 |
| Cu | 50.83 |
| Ag | 0.13 |
| Fe | 0.19 |
| O | 0.003 |

**Fig. 15.** APT elemental maps for the first prepared tip from the $Cu_6Sn_5$ intermetallic layer close to the interface with $Cu_3Sn$.

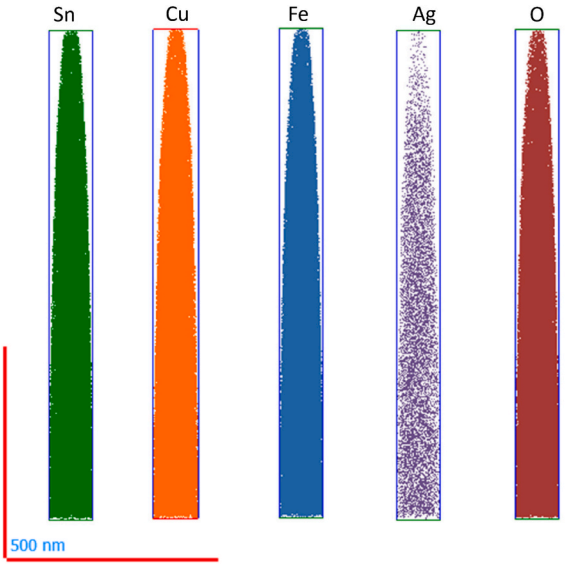


Tip Number: M28
LEAP Run: R52_17693
Ions: 136M

| Element | at. % |
|---|---|
| Sn | 47.36 |
| Cu | 51.43 |
| Ag | 0.12 |
| Fe | 0.713 |
| O | 0.014 |

**Fig. 16.** APT elemental maps for the second tip from the $Cu_6Sn_5$ layer near the solder alloy matrix.

composition semi-phases and the solder alloy matrix. Regarding the interesting results reported in Fig. 19, it is worth noting that indexed SAED patterns of the secondary-phase nanoscale precipitates, together with their crystallography, and the elemental maps from STEM/EDS and APT analyses presented earlier, confirm that the dominant intermetallic phase between iron and tin is $FeSn_2$.

## 4. Conclusions

The innovation of this research lies in providing valuable insights into the atomic-level structures of $Cu_3Sn$ and $Cu_6Sn_5$ intermetallic layers within solder joints using advanced characterization techniques, including FIB/STEM, APT, and NBDM analyses. This study provides new microstructural details and atomistic mechanisms for these intermetallic compounds and their interactions with iron nanoparticles during reflow solidification and subsequent aging heat treatments.

The key findings are as follows:

- The Cu/$Cu_3Sn$ interface exhibits a well-defined metallurgical bond, characterized by a thin nanometric layer formation on the copper substrate. The $Cu_3Sn$ layer exhibits an ultra-fine-grained structure, with grain sizes ranging from 200 to 500 nm.
- A diffusive interface is formed, undergoing the subsequent $Cu_6Sn_5$ intermetallic phase growth across the $Cu_3Sn$ layer's boundary. This results in a sharp transition from the nano-grained structure of $Cu_3Sn$ to the coarse-grained microstructure of $Cu_6Sn_5$.
- The localized segregation of iron within the $Cu_3Sn$ intermetallic layer, as analyzed by EDS elemental mapping and APT atomic-level

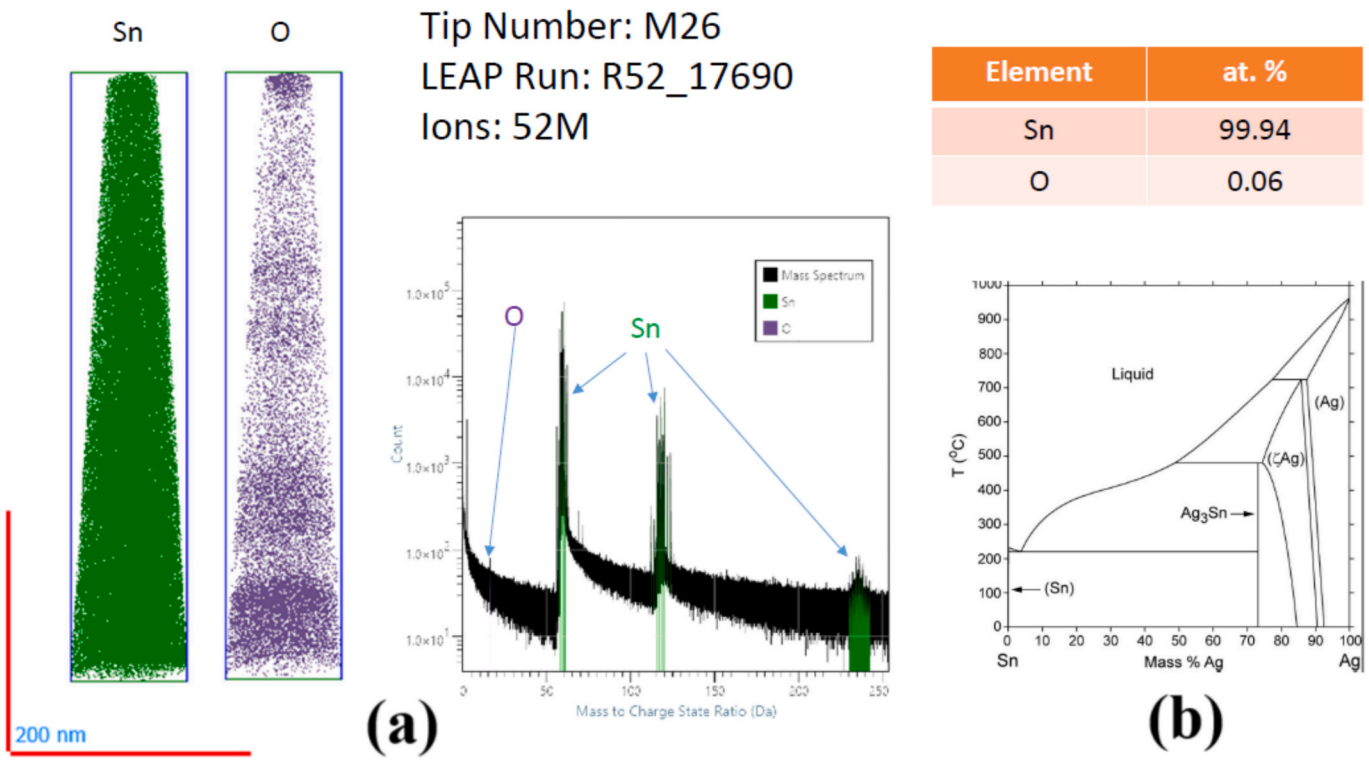


**Fig. 17.** (a) APT elemental analysis of the tip prepared from the solder alloy matrix close to the intermetallic layer after reflow soldering and thermal aging. (b) The corresponding Sn-Ag phase diagram [84,85].

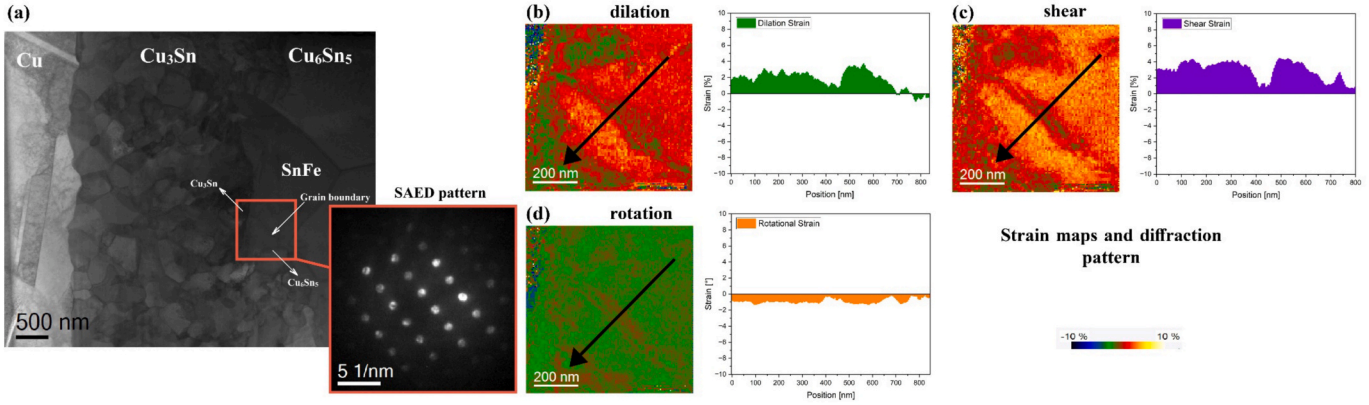


**Fig. 18.** Nano-scale strain mapping for the interface region between $Cu_3Sn$ and $Cu_6Sn_5$ intermetallic phases by NBDM: (a) BF-STEM image combined with the corresponding SAED pattern. Contour maps and distribution plots for the (b) dilation, (c) shear, and (d) rotation strains across the boundary of two phases.

chemical analysis, reveals a trapping mechanism of iron that slows the $Cu_3Sn$ phase growth kinetics.

- Addition of iron nanoparticles via doped flux across the solder joint interface influences growth kinetics for $Cu_3Sn$ phase toward the solder alloy region, manifesting in three major contributions at different locations. First, the solid solution of iron in the $Cu_6Sn_5$ phase could affect its crystal structure, as shown by STEM NBDM analysis. This mechanism is most prominent near the interface with the $Cu_3Sn$ layer (based on the APT maps). Second, nanoscale $FeSn_2$ intermetallic phase precipitation occurs via *in situ* chemical reactions between iron nanoparticles and tin, acting as a retarding mechanism on the growth of the $Cu_6Sn_5$ phase and shaping its leading edge during reflow solidification and thermal aging. Third, the dragging of iron solutes at the $Cu_6Sn_5$/Sn interface during solidification and age-coarsening alters the eutectic phase structure, further suppressing the progression of the intermetallic layer.
- Nanoscale strain distribution maps, determined using NBDM, reveal significant localized shear strain variations at the interface between phases, particularly at the $Cu_3Sn/Cu_6Sn_5$ boundary, highlighting the influence of intermetallic phase transitions on strain distribution within the matrix, while these internal stresses can control the subsequent failure performance of lead-free solder joints.

## CRediT authorship contribution statement

**Farzad Khodabakhshi:** Writing – review & editing, Writing – original draft, Visualization, Validation, Supervision, Software, Methodology, Investigation, Formal analysis, Data curation, Conceptualization. **Irina Wodak:** Investigation. **Shabnam Taheriniya:** Investigation. **Andriy Yakymovych:** Investigation. **Michael K. Eusterholz:** Investigation. **Gerhard Wilde:** Writing – review & editing, Supervision, Resources, Funding acquisition, Conceptualization. **Golta Khatibi:**

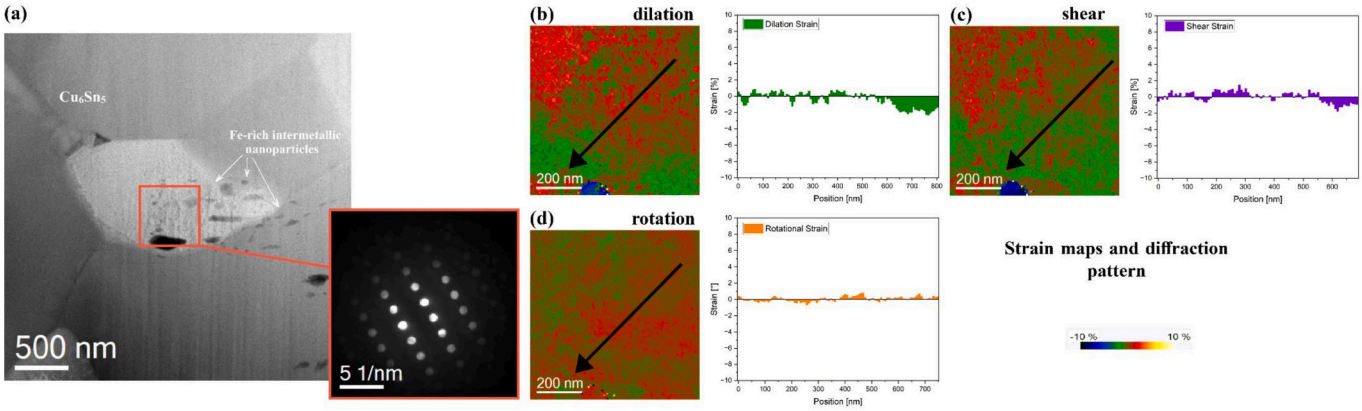


**Fig. 19.** Nano-scale strain distribution around the Fe-rich intermetallic nanoparticles dispersed through the $Cu_6Sn_5$ intermetallic phase matrix: (a) BF-STEM microstructure showing the selected region for nano-beam diffraction strain calculations, (b) dilation, (c) shear, and (d) rotation strain variations in two forms of contour plots and distribution curves.

Writing – review & editing, Supervision, Resources, Project administration, Funding acquisition, Conceptualization.

## Declaration of competing interest

The authors declare that they have no known competing financial interests or personal relationships that could have appeared to influence the work reported in this paper.

## Acknowledgements

The financial support by the Austrian Science Foundation (FWF) under the grant number P-34894 is gratefully acknowledged. Also, the authors acknowledge Karlsruhe Nano Micro Facility (KNMF) for providing advanced instruments (proposal number: 2024-031-031972). FKH and GW would also like to acknowledge support under the scheme for project 101155568 — SHSBALMBNA — HORIZON-MSCA-2023-PF-01. This project was partially supported for the accomplishment of APT experiments by Karlsruhe Nano Micro Facility (KNMFi) at Karlsruhe Institute of Technology (KIT), proposal 2024-031-031972.

## Data availability

Data will be made available on request.

## References

[1] L. Ai, W. Lin, C. Cao, P. Li, X. Wang, D. Lv, X. Li, Z. Yang, X. Yao, Tough soldering for stretchable electronics by small-molecule modulated interfacial assemblies, *Nat*, Commun 14 (1) (2023).
[2] J.W. Xian, Y.L. Xu, S. Stoyanov, R.J. Coyle, F.P.E. Dunne, C.M. Gourlay, The role of microstructure in the thermal fatigue of solder joints, *Nat*, Commun 15 (1) (2024).
[3] J. Gong, C. Liu, P.P. Conway, V.V. Silberschmidt, Evolution of CuSn intermetallics between molten SnAgCu solder and Cu substrate, Acta Mater. 56 (16) (2008) 4291–4297.
[4] M.S. Park, M.K. Stephenson, C. Shannon, L.A. Cáceres Díaz, K.A. Hudspeth, S. L. Gibbons, J. Muñoz-Saldaña, R. Arróyave, Experimental and computational study of the morphological evolution of intermetallic compound ($Cu_6Sn_5$) layers at the Cu/Sn interface under isothermal soldering conditions, Acta Mater. 60 (13–14) (2012) 5125–5134.
[5] M.S. Park, R. Arróyave, Concurrent nucleation, formation and growth of two intermetallic compounds ($Cu_6Sn_5$ and $Cu_3Sn$) during the early stages of lead-free soldering, Acta Mater. 60 (3) (2012) 923–934.
[6] J.F. Li, P.A. Agyakwa, C.M. Johnson, Interfacial reaction in Cu/Sn/Cu system during the transient liquid phase soldering process, Acta Mater. 59 (3) (2011) 1198–1211.
[7] K.H. Prakash, T. Sritharan, Interface reaction between copper and molten tin-lead solders, Acta Mater. 49 (13) (2001) 2481–2489.
[8] M.S. Park, R. Arróyave, Early stages of intermetallic compound formation and growth during lead-free soldering, Acta Mater. 58 (14) (2010) 4900–4910.
[9] J.O. Suh, K.N. Tu, G.V. Lutsenko, A.M. Gusak, Size distribution and morphology of $Cu_6Sn_5$ scallops in wetting reaction between molten solder and copper, Acta Mater. 56 (5) (2008) 1075–1083.
[10] J. Keller, D. Baither, U. Wilke, G. Schmitz, Mechanical properties of Pb-free SnAg solder joints, Acta Mater. 59 (7) (2011) 2731–2741.
[11] Y. Yao, X. He, L.M. Keer, M.E. Fine, A continuum damage mechanics-based unified creep and plasticity model for solder materials, Acta Mater. 83 (2015) 160–168.
[12] Q.K. Zhang, Z.F. Zhang, *In situ* observations on creep fatigue fracture behavior of Sn-4Ag/Cu solder joints, Acta Mater. 59 (15) (2011) 6017–6028.
[13] J. Görlich, D. Baither, G. Schmitz, Reaction kinetics of Ni/Sn soldering reaction, Acta Mater. 58 (9) (2010) 3187–3197.
[14] M. Kerr, N. Chawla, Creep deformation behavior of Sn-3.5Ag solder/Cu couple at small length scales, Acta Mater. 52 (15) (2004) 4527–4535.
[15] F. Che Ani, A. Jalar, A.A. Saad, C.Y. Khor, R. Ismail, Z. Bachok, M.A. Abas, N. K. Othman, The influence of $Fe_2O_3$ nano-reinforced SAC lead-free solder in the ultra-fine electronics assembly, *J*, Adv. Manuf. Technol. 96 (1–4) (2018) 717–733.
[16] S. Chellvarajoo, M.Z. Abdullah, Z. Samsudin, Effects of $Fe_2NiO_4$ nanoparticles addition into lead-free Sn-3.0Ag-0.5Cu solder pastes on microstructure and mechanical properties after reflow soldering process, Mater. Des. 67 (2015) 197–208.
[17] Y. Gu, X. Zhao, Y. Li, Y. Liu, Y. Wang, Z. Li, Effect of nano-$Fe_2O_3$ additions on wettability and interfacial intermetallic growth of low-Ag content Sn-Ag-Cu solders on Cu substrates, J. Alloys Compd. 627 (2015) 39–47.
[18] X. Zhao, Y. Wen, Y. Li, Y. Liu, Y. Wang, Effect of γ-$Fe_2O_3$ nanoparticles size on the properties of Sn-1.0Ag-0.5Cu nano-composite solders and joints, J. Alloys Compd. 662 (2016) 272–282.
[19] S. Shang, A. Kunwar, J. Yao, Y. Wang, H. Ma, Y. Wang, Effect of the $TiO_2$ Nanoparticles on the Growth Behavior of Intermetallics in Sn/Cu Solder Joints, Met. Mater. Int. 25 (2) (2019) 499–507.
[20] S. Kim, K.S. Kim, S.S. Kim, K. Suganuma, G. Izuta, Improving the reliability of Si die attachment with Zn-Sn-based high-temperature Pb-free solder using a TiN diffusion barrier, J. Electron. Mater. 38 (12) (2009) 2668–2675.
[21] M.A.A. Mohd Salleh, A.M.M.A. Bakri, M.H. Zan Hazizi, F. Somidin, N.F. Mohd Alui, Z.A. Ahmad, Mechanical properties of Sn-0.7Cu/$Si_3N_4$ lead-free composite solder, Mater. Sci. Eng. A 556 (2012) 633–637.
[22] M.A.A. Mohd Salleh, A.M. Mustafa Al Bakri, H. Kamarudin, M. Bnhussain, F. Somidin, Solderability of Sn-0.7Cu/$Si_3N_4$ lead-free composite solder on Cu-substrate, *Phys*, Procedia (2011) 299–304.
[23] A.A. El-Daly, W.M. Desoky, T.A. Elmosalami, M.G. El-Shaarawy, A.M. Abdraboh, Microstructural modifications and properties of SiC nanoparticles-reinforced Sn-3.0Ag-0.5Cu solder alloy, Mater. Des. 65 (2015) 1196–1204.
[24] A.A. El-Daly, A. Fawzy, S.F. Mansour, M.J. Younis, Novel SiC nanoparticles-containing Sn-1.0Ag-0.5Cu solder with good drop impact performance, *Mater*, Sci. Eng. A 578 (2013) 62–71.
[25] P. Liu, P. Yao, J. Liu, Effect of SiC nanoparticle additions on microstructure and microhardness of Sn-Ag-Cu solder alloy, J. Electron. Mater. 37 (6) (2008) 874–879.
[26] X. Wang, Y.C. Liu, C. Wei, H.X. Gao, P. Jiang, L.M. Yu, Strengthening mechanism of SiC-particulate reinforced Sn-3.7Ag-0.9Zn lead-free solder, J. Alloys Compd. 480 (2) (2009) 662–665.
[27] N.S. Javid, R. Sayyadi, F. Khodabakhshi, Lead-free Sn-based/MW-CNTs nanocomposite soldering: effects of reinforcing content, Ni-coating modification, and isothermal ageing treatment, J. Mater. Sci. Mater. Electron. 30 (2019) 4737–4752.
[28] F. Khodabakhshi, R. Sayyadi, N.S. Javid, Lead free Sn-Ag-Cu solders reinforced by Ni-coated graphene nanosheets prepared by mechanical alloying: Microstructural evolution and mechanical durability, Mater. Sci. Eng. A 702 (2017) 371–385.
[29] F. Khodabakhshi, M. Zareghomsheh, G. Khatibi, Nanoindentation creep behavior of SAC-based lead-free nanocomposite solders reinforced by Ni-coated MW-CNTs, Mater. Sci. Eng. A 797 (140203) (2020) 1–15.

[30] R. Sayyadi, F. Khodabakhshi, N.S. Javid, G. Khatibi, Influence of graphene content and nickel decoration on the microstructural and mechanical characteristics of the Cu/Sn–Ag–Cu/Cu soldered joint, J. Mater. Res. Technol. 9 (4) (2020) 8953–8970.
[31] G.K. Sujan, A.S.M.A. Haseeb, A.B.M. Afifi, Effects of metallic nanoparticle doped flux on the interfacial intermetallic compounds between lead-free solder ball and copper substrate, Mater Charact 97 (2014) 199–209.
[32] M. Aamir, R. Muhammad, M. Tolouei-Rad, K. Giasin, V.V. Silberschmidt, A review: microstructure and properties of tin-silver-copper lead-free solder series for the applications of electronics, Solder. Surf. Mount Tech. 32 (2) (2020) 115–126.
[33] S. Chellvarajoo, M.Z. Abdullah, Investigation on nano-reinforced solder paste after reflow soldering part 1: Effects of nano-reinforced solder paste on melting, hardness, spreading rate, and wetting quality, Microelectron. Reliab. 84 (2018) 230–237.
[34] N. Lu, D. Yang, L. Li, Interfacial reaction between Sn-Ag-Cu solder and Co-P films with various microstructures, Acta Mater. 61 (12) (2013) 4581–4590.
[35] Y. Yang, J.N. Balaraju, Y. Huang, H. Liu, Z. Chen, Interface reaction between an electroless Ni-Co-P metallization and Sn-3.5Ag lead-free solder with improved joint reliability, Acta Mater. 71 (2014) 69–79.
[36] T. Ventura, S. Terzi, M. Rappaz, A.K. Dahle, Effects of Ni additions, trace elements and solidification kinetics on microstructure formation in Sn-0.7Cu solder, Acta Mater. 59 (10) (2011) 4197–4206.
[37] D.C. Lin, C.Y. Kuo, T.S. Srivatsan, M. Petraroli, G.X. Wang, Synthesis and characterization of nano-composite lead-free solder, *J Metastable Nanocryst*, Mater (2005) 145–148.
[38] S. Xu, A.H. Habib, A.D. Pickel, M.E. McHenry, Magnetic nanoparticle-based solder composites for electronic packaging applications, Prog. Mater Sci. 67 (2015) 95–160.
[39] H.R. Kotadia, P.D. Howes, S.H. Mannan, A review: on the development of low melting temperature Pb-free solders, Microelectron. Reliab. 54 (6–7) (2014) 1253–1273.
[40] M.M.A. Mohd Salleh, S. McDonald, K. Nogita, Non-metal reinforced lead-free composite solder fabrication methods and its reinforcing effects to the suppression of intermetallic formation: short review, *Appl*, Mech. Mater. (2013) 260–266.
[41] J. Shen, Y.C. Chan, Research advances in nano-composite solders, Microelectron. Reliab. 49 (3) (2009) 223–234.
[42] J. Shen, Y.C. Chan, Effect of metal/ceramic nanoparticle-doped fluxes on the wettability between Sn-Ag-Cu solder and a Cu layer, J. Alloys Compd. 477 (1–2) (2009) 909–914.
[43] H. Wang, X. Hu, Q. Li, M. Qu, Effect of flux doped with $Cu_6Sn_5$ nanoparticles on the interfacial reaction of lead-free solder joints, J. Mater. Sci. Mater. Electron. 30 (12) (2019) 11552–11562.
[44] I. Wodak, F. Khodabakhshi, A. Yakymovych, G. Khatibi, Microstructural Features and Crystallographic Texture of Sn3. 5Ag Solder Joints Produced with Fe-Nanoparticle Doped Flux, IEEE (2023).
[45] Z. Gui, X. Hu, X. Jiang, Y. Li, H. Wang, Interfacial reaction, wettability, and shear strength of ultrasonic-assisted lead-free solder joints prepared using Cu–GNSs-doped flux, J. Mater. Sci. Mater. Electron. 32 (19) (2021) 24507–24523.
[46] S. Shang, A. Kunwar, Y. Wang, J. Yao, Y. Wu, H. Ma, Y. Wang, Geometrical Effects of Cu@Ag Core–Shell Nanoparticles Treated Flux on the Growth Behaviour of Intermetallics in Sn/Cu Solder Joints, Electron. Mater. Lett. 15 (2) (2019) 253–265.
[47] S. Shang, Y. Wang, Y. Wang, H. Ma, A. Kunwar, Enhancement of hardness of bulk solder by doping Cu nanoparticles at the interface of Sn/Cu solder joint, Microelectron. Eng. 208 (2019) 47–53.
[48] M.N. Bashir, A.S.M.A. Haseeb, Grain size stability of interfacial intermetallic compound in Ni and Co nanoparticle-doped SAC305 solder joints under electromigration, J. Mater. Sci. Mater. Electron. 33 (17) (2022) 14240–14248.
[49] M.N. Bashir, A.S.M.A. Haseeb, A.Z.M.S. Rahman, M.A. Fazal, Effect of Cobalt Doping on the Microstructure and Tensile Properties of Lead Free Solder Joint Subjected to Electromigration, J. Mater. Sci. Technol. 32 (11) (2016) 1129–1136.
[50] M.N. Bashir, A.S.M.A. Haseeb, S. Wakeel, M.A. Khan, M.M. Quazi, N.B. Khan, A. Ahmed, M.E.M. Soudagar, Effect of Ni and Co nanoparticle-doped flux on microstructure of SAC305 solder matrix, J. Mater. Sci. Mater. Electron. 33 (25) (2022) 20106–20120.
[51] G.K. Sujan, A.S.M.A. Haseeb, H. Nishikawa, M.A. Amalina, Interfacial reaction, ball shear strength and fracture surface analysis of lead-free solder joints prepared using cobalt nanoparticle doped flux, J. Alloys Compd. 695 (2017) 981–990.
[52] M.N. Bashir, N.B. Khan, S. Bashir, A.F. Khan, M.M. Quazi, M. Gul, S. Wakeel, H. M. Saad, Effect of Zn nanoparticle-doped flux on mechanical properties of SAC305 solder joint after electromigration, J. Mater. Sci. Mater. Electron. 34 (4) (2023).
[53] M. He, Z. Chen, G. Qi, Solid state interfacial reaction of Sn-37Pb and Sn-3.5Ag solders with Ni-P under bump metallization, Acta Mater. 52 (7) (2004) 2047–2056.
[54] M.N. Bashir, A.S.M.A. Haseeb, Improving mechanical and electrical properties of Cu/SAC305/Cu solder joints under electromigration by using Ni nanoparticles doped flux, J. Mater. Sci. Mater. Electron. 29 (4) (2018) 3182–3188.
[55] M.N. Bashir, A.S.M.A. Haseeb, A.Z.M.S. Rahman, M.A. Fazal, C.R. Kao, Reduction of electromigration damage in SAC305 solder joints by adding Ni nanoparticles through flux doping, J. Mater. Sci. 50 (20) (2015) 6748–6756.
[56] H. Wang, X. Hu, X. Jiang, Y. Li, Interfacial reaction and shear strength of ultrasonically-assisted Sn-Ag-Cu solder joint using composite flux, J. Manuf. Process. 62 (2021) 291–301.
[57] M. Maleki, J. Cugnoni, J. Botsis, Microstructure-based modeling of the ageing effect on the deformation behavior of the eutectic micro-constituent in SnAgCu lead-free solder, Acta Mater. 61 (1) (2013) 103–114.
[58] B. Chao, S.H. Chae, X. Zhang, K.H. Lu, J. Im, P.S. Ho, Investigation of diffusion and electromigration parameters for Cu-Sn intermetallic compounds in Pb-free solders using simulated annealing, Acta Mater. 55 (8) (2007) 2805–2814.
[59] W.T. Lin, C.J. Hsu, P.K. Chang, K. Li, K.S. Lin, C.M. Wang, A.T. Wu, Microstructural Evolution, Mechanical Properties, and thermal Reliability of Bi- and Ni-Doped Sn-Ag-based Lead-Free Solder Alloys, JOM (2026).
[60] Z. Wu, W. Chen, S. Tan, X. Jiang, X. Hu, Synergistic enhancement of Sn-based solders through silver-graphene nanosheets and ultrasound assistance: Interface reactions, crystal orientation, mechanical properties, Mater Charact 229 (2025).
[61] Y. Xiang, B. Wang, J. Xu, J. Yan, Effect of Ni content on interfacial structure and tensile strength of SACSBN/Cu solder joints, Weld. World (2026).
[62] A. Durga, P. Wollants, N. Moelans, Phase-field study of IMC growth in Sn–Cu/Cu solder joints including elastoplastic effects, Acta Mater. 188 (2020) 241–258.
[63] M.B. Kelly, S. Niverty, N. Chawla, Four-dimensional (4D) microstructural evolution of $Cu_6Sn_5$ intermetallic and voids under electromigration in bi-crystal pure Sn solder joints, Acta Mater. 189 (2020) 118–128.
[64] Y.W. Chang, Y. Cheng, F. Xu, L. Helfen, T. Tian, M. Di Michiel, C. Chen, K.N. Tu, T. Baumbach, Study of electromigration-induced formation of discrete voids in flip-chip solder joints by *in-situ* 3D laminography observation and finite-element modeling, Acta Mater. 117 (2016) 100–110.
[65] M.S. Park, S.L. Gibbons, R. Arróyave, Phase-field simulations of intermetallic compound evolution in Cu/Sn solder joints under electromigration, Acta Mater. 61 (19) (2013) 7142–7154.
[66] S. Ka, D. Bae, A. Sharma, J.P. Jung, H.S. Kim, Laser solder ball jetting of SAC305/ENIG joints: Microstructure, kinetics, and reliability under multiple reflow cycles, Intermetallics 189 (2026).
[67] J. Liu, J. Xu, S. Yi, X. Li, H. Tan, B. Wang, J. Yan, Effect of Ti content on the microstructure evolution and solder joint reliability of SAC305-2.0Sb-3.0Bi-0.1Ni lead-free solder alloy, *J*, Mater. Sci. Mater. Electron. 37 (6) (2026).
[68] B. Wang, J. Zhao, Y. Xiang, Q. He, F. Li, S. Zhang, J. Wang, J. Yan, The synergistic inhibition of the growth of intermetallic compounds at SAC305/Cu interface by Ni and Bi, Mater Charact 232 (2026).
[69] Z. Liang, Formation and growth mechanism of thin $Cu_6Sn_5$ films in Sn/Cu and Sn-0.1AlN/Cu structures using laser heating, Solder. Surf. Mount Tech. 36 (5) (2024) 268–275.
[70] S. Li, X. Wang, M. Liao, Z. Li, Q. Li, H. Yan, A. Liu, F. Wang, Microstructures, mechanical properties, and reliability induced from size effect in Sn-based solder joints: Review, J. Mater. Res. Technol. 35 (2025) 5067–5083.
[71] J. Huang, W. Hu, Y. Tian, L. Yin, H. Zhang, G. Wang, Synergistic modification of Sn-9Zn solder using nano-SiC-based interface-active multifunctional reinforcements, Mater Charact 230 (2025).
[72] F. Khodabakhshi, I. Wodak, A. Yakymovych, S. Taheriniya, S. Khademorezaian, G. Wilde, G. Khatibi, Nano-scale mechanistic model for microstructural reliability in reactive hybrid solder joints, Mater Charact 216 (2024) 114247.
[73] T. Ventura, S. Terzi, M. Rappaz, A.K. Dahle, Effects of solidification kinetics on microstructure formation in binary Sn-Cu solder alloys, Acta Mater. 59 (4) (2011) 1651–1658.
[74] ASM Handbook Volume 6: Welding, Brazing, and Soldering.
[75] G. Humpston, D.M. Jacobson, Principles of soldering and brazing, ASM International, Materials Park, OH, 1993.
[76] G. Ghosh, Interfacial microstructure and the kinetics of interfacial reaction in diffusion couples between Sn-Pb solder and Cu/Ni/Pd metallization, Acta Mater. 48 (14) (2000) 3719–3738.
[77] D. Gupta, K. Vieregge, W. Gust, Interface diffusion in eutectic Pb-Sn solder, Acta Mater. 47 (1) (1998) 5–12.
[78] B.J. Lee, N.M. Hwang, H.M. Lee, Prediction of interface reaction products between Cu and various solder alloys by thermodynamic calculation, Acta Mater. 45 (5) (1997) 1867–1874.
[79] Y.X. Gao, H. Fan, Z. Xiao, Thermodynamics model for solder profile evolution, Acta Mater. 48 (4) (2000) 863–874.
[80] Y. Cui, J.W. Xian, A. Zois, K. Marquardt, H. Yasuda, C.M. Gourlay, Nucleation and growth of $Ag_3Sn$ in Sn-Ag and Sn-Ag-Cu solder alloys, Acta Mater. 249 (2023).
[81] J.F. Li, P.A. Agyakwa, C.M. Johnson, Kinetics of $Ag_3Sn$ growth in Ag-Sn-Ag system during transient liquid phase soldering process, Acta Mater. 58 (9) (2010) 3429–3443.
[82] O.Y. Liashenko, S. Lay, F. Hodaj, On the initial stages of phase formation at the solid Cu/liquid Sn-based solder interface, Acta Mater. 117 (2016) 216–227.
[83] R.K. Chinnam, C. Fauteux, J. Neuenschwander, J. Janczak-Rusch, Evolution of the microstructure of Sn-Ag-Cu solder joints exposed to ultrasonic waves during solidification, Acta Mater. 59 (4) (2011) 1474–1481.
[84] C.S. Oh, J.H. Shim, B.J. Lee, L. Dong Nyung, A thermodynamic study on the Ag-Sb-Sn system, J. Alloys Compd. 238 (1) (1996) 155–166.
[85] W. Gierlotka, Thermodynamic Description of the Quaternary Ag-Cu-In-Sn System, J. Electron. Mater. 41 (1) (2012) 86–108.